NREL/TP-451-5591 • UC Category: 270 • DE93017115

High Efficiency Epitaxial Optical Reflector Solar Cells

Final Subcontract Report
1 January 1990 – 31 October 1992

P. Daniel Dapkus
Steven G. Hummel
University of Southern California
Los Angeles, California

NREL technical monitor: T. Basso

National Renewable Energy Laboratory
1617 Cole Boulevard
Golden, Colorado 80401-3393
Operated by Midwest Research Institute
for the U.S. Department of Energy
under Contract No. DE-AC02-83CH10093

Prepared under Subcontract No. XM-0-18110-3

August 1993

MASTER

DISTRIBUTION OF THIS DOCUMENT IS UNLIMITED

This publication was reproduced from the best available camera-ready copy
submitted by the subcontractor and received no editorial review at NREL.

NOTICE

NOTICE: This report was prepared as an account of work sponsored by an agency of the United States government. Neither the United States government nor any agency thereof, nor any of their employees, makes any warranty, express or implied, or assumes any legal liability or responsibility for the accuracy, completeness, or usefulness of any information, apparatus, product, or process disclosed, or represents that its use would not infringe privately owned rights. Reference herein to any specific commercial product, process, or service by trade name, trademark, manufacturer, or otherwise does not necessarily constitute or imply its endorsement, recommendation, or favoring by the United States government or any agency thereof. The views and opinions of authors expressed herein do not necessarily state or reflect those of the United States government or any agency thereof.

Printed in the United States of America
Available from:
National Technical Information Service
U.S. Department of Commerce
5285 Port Royal Road
Springfield, VA 22161

Price: Microfiche A01
Printed Copy A04

Codes are used for pricing all publications. The code is determined by the number of pages in the publication. Information pertaining to the pricing codes can be found in the current issue of the following publications which are generally available in most libraries: *Energy Research Abstracts (ERA); Government Reports Announcements and Index (GRA and I); Scientific and Technical Abstract Reports (STAR);* and publication NTIS-PR-360 available from NTIS at the above address.

Printed on recycled paper

DISCLAIMER

Portions of this document may be illegible electronic image products. Images are produced from the best available original document.

Table of Contents

1.0 Introduction 2

2.0 Cell Concept 2

3.0 Summary of Results 6

Task 1: Solar Cell and Reflector Modeling 6
Task 2: Materials Growth and Optimization 21
Task 3: Solar Cell Fabrication and Characterization 32

4.0 Summary and Conclusions 45

5.0 Recommendations 47

Final Report – EOR Solar Cell

1.0 Introduction

The objective of this program is to test the feasibility of a new solar cell concept – the epitaxial optical reflector (EOR) solar cell. This cell concept alters current designs for high efficiency cells by changing the optical absorption efficiency of single cells. The change is introduced by the use of an epitaxial multilayer reflector as an integral part of the cell to increase the optical path length of certain wavelengths of light in the cell. These changes are expected to increase the open circuit voltage at which power is extracted from the cell.

The program is designed to test the feasibility of the use of a broad band epitaxial multilayer reflector grown as an integral part of the device structure to reflect the near-band-edge light back through the device for a second absorption pass. This second pass allows one to design a solar cell with a thinner base and to use the epitaxial reflector as a heterojunction carrier-reflecting barrier at the rear of the device. The thinner cell design and altered carrier profile that results from the light- and carrier-reflecting barrier will decrease the carrier concentration gradient and increase the open circuit voltage. These effects will be described in detail in the following section.

The program is structured to have three tasks: 1.) Solar Cell and Reflector Modelling, 2.) Materials Growth and Optimization, and 3.) Solar Cell Fabrication and Characterization. The initial plan placed USC's efforts centered on Tasks 1 and 2, with Task 3 performed in collaboration with Varian Research center for high efficiency cell fabrication. Although we have the facilities to fabricate solar cells, it was felt that the concept could only be proved by the demonstration of cell efficiencies higher than that achievable with current technology. It was also felt that the level of effort was insufficient on this program to develop all aspects of the device technology to a sufficient level to demonstrate the high efficiency necessary. Unfortunately, Varian eliminated its efforts in solar cell technology, and all three tasks were completed by USC.

2.0 Cell Concept

In the conventional GaAs solar cell of Fig. 1, the minimum active region thickness is designed to be approximately approximately three times thicker than the absorption depth of the longest wavelength photon absorbed by the cell.

This usually means that the active region of a solar cell made from a direct band gap material such as GaAs must be 3 - 4 µm thick. This design rule allows the red and infrared radiation to be efficiently absorbed before passing comletely through the base region while the higher energy radiation is absorbed in the emitter and space charge region. The cell efficiency then relies on the efficient collection of the minority carriers generated in the base and emitter regions. This can be improved in the conventional cell by promoting carrier diffusion towards the p-n junction with doping and composition gradients in the base region and to a lesser extent with a heterojunction barrier at the back of the base layer. The heterojunction barrier would be more effective in improving the minority carrier collection efficiency and the open circuit voltage if the base region of the device was made thinner. Unfortunately, this results in fewer photons being absorbed.

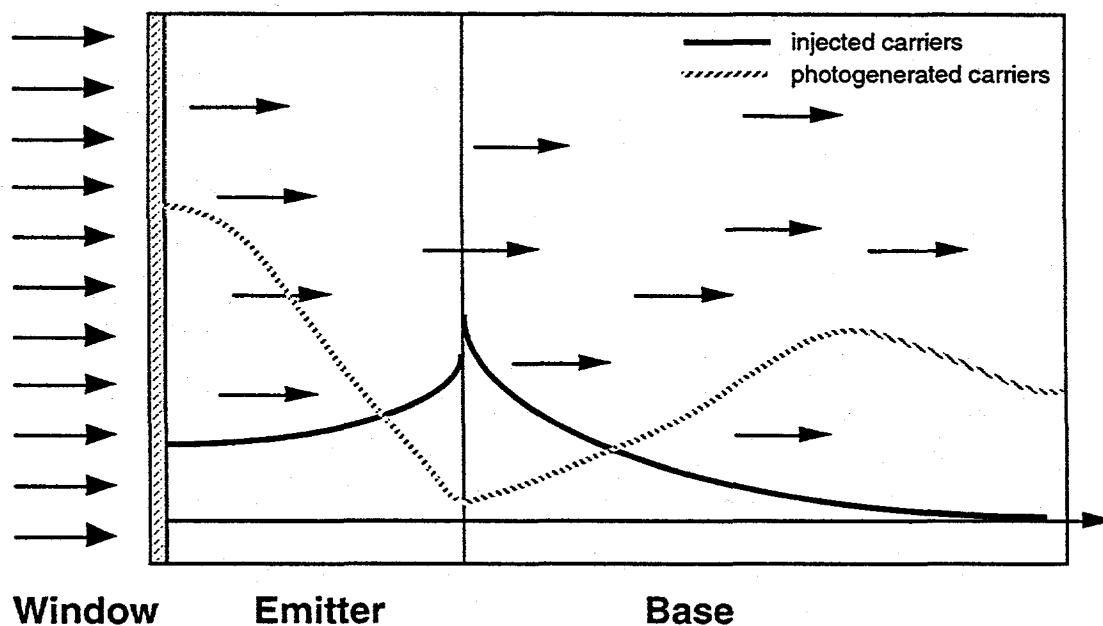

Fig. 1 Schematic diagram of conventional solar cell showing carrier distributions.

The cell design we have proposed allows the effective use of thinner layers and heterojunction confining barriers by monolithically incorporating a high reflectivity multilayer optical reflector at the rear of the base region. The optical reflector is formed from a multilayer epitaxial structure of materials with different refractive indices but with the same lattice constant. For this reason we refer to the cell as the epitaxial optical reflector cell (EOR cell). The cell concept is shown schematically in Fig. 2. The optical reflector is designed to be selectively reflective to the longer wavelength photons that would normally be inefficiently absorbed by a thin cell. These photons are reflected

back through the cell for a second pass and complete absorption. The presence of this reflector allows one to design a cell in which the active layers are thin enough that a heterojunction barrier at the rear of the cell alters the distribution of both the injected and photogenerated carriers in the structure in such a way as to improve the efficiency and, incidentally, the radiation hardness. The distribution of minority carriers due to solar photogeneration are shown in Figs. 1 and 2 and the distribution of injected minority carriers due to the forward bias of the device are shown in Figs. 3 and 4 respectively.

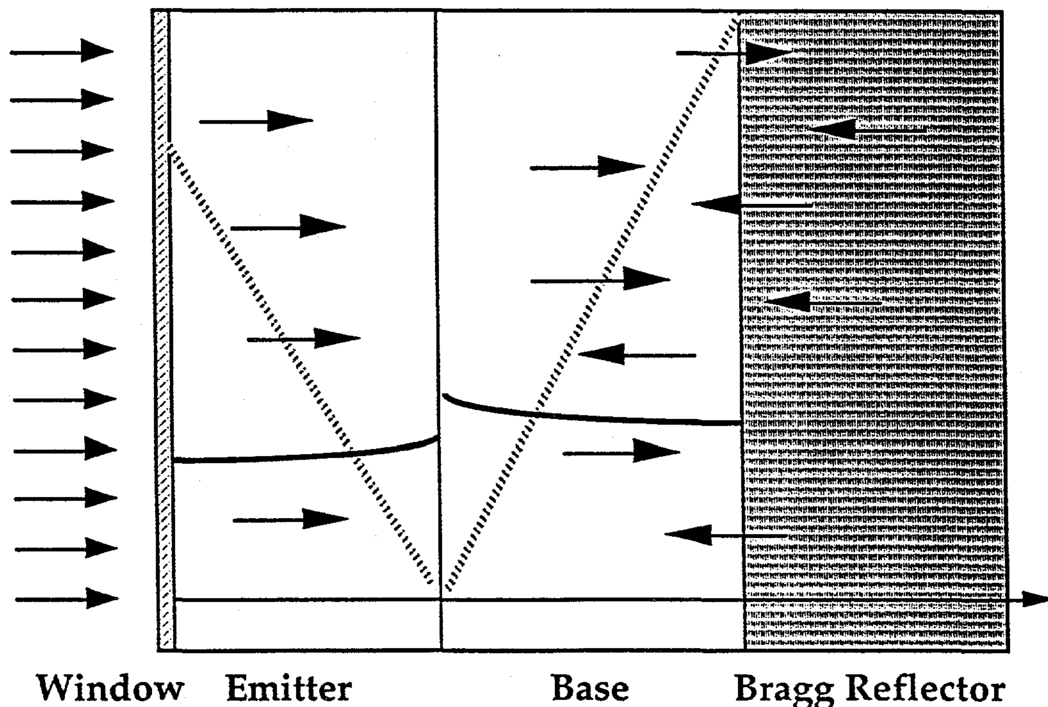

Fig. 2 Schematic Diagram of EOR solar cell showing carrier distributions.

The presence of the heterojunction at the rear of the base impedes the back-diffusion of photogenerated carriers and, because the base thickness can now be comparable to the diffusion length of the carriers in the base, it establishes a **carrier gradient that is controlled by the device structure** rather than the minority carrier diffusion length. In addition, **the distribution of injected minority carriers at a given bias is substantially flattened by the presence of the heterobarrier.** In a cell in which diffusion currents dominate the saturation current at the operating point, this leads toreduced diffusion current at a given bias and higher open circuit voltage at a given photocurrent, as shown below:

$$I_{diff} = qA\left(D_n \frac{dn_p}{dx} + D_p \frac{dp_n}{dx}\right)\Bigg|_{x=0} \quad (1)$$

$$V_{oc} = \frac{kT}{q}\left\{\ln\left(\frac{I_{phot}}{I_{odiff}}\right) + 1\right\} \quad (2)$$

Since the minority carrier gradients in (1) are substantially reduced, the diffusion saturation current of (2) is also reduced and results in a higher V_{OC}.

Base Carrier Distributions

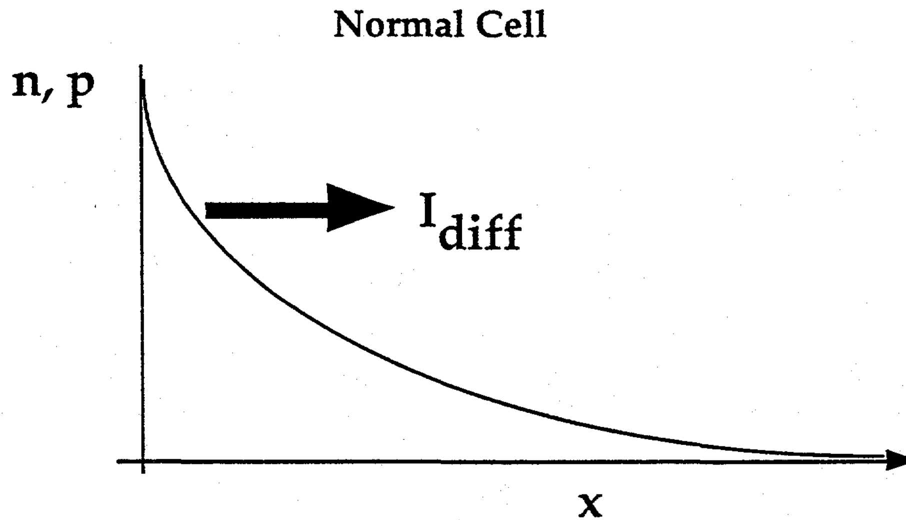

Fig. 3 Schematic diagram of base carrier distribution and resulting current for conventional solar cell.

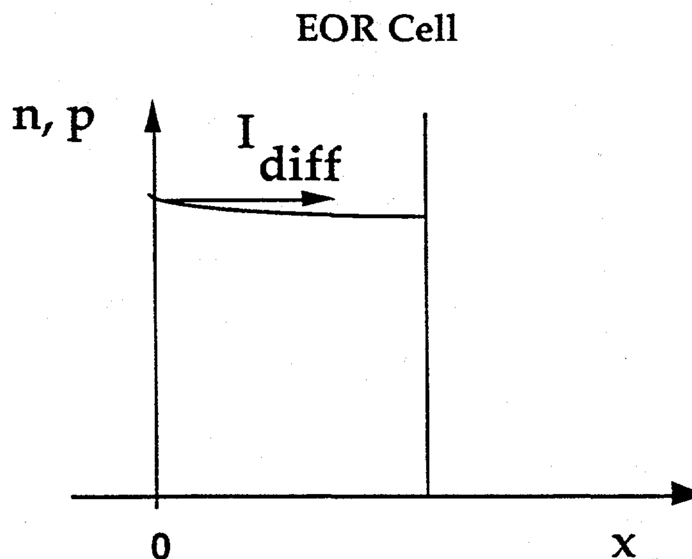

Fig. 4 Base carrier distribution and resulting current for EOR solar cell.

3.0 Summary of Results

Task 1: Solar Cell and Reflector Modelling

An early issue in the discussion of this concept relates to one's ability to construct the required reflector. To place this discussion in proper context, it is necessary to consider the spectral range the reflector would have to span. In Fig.5, we show the calculated absorption coefficient of GaAs based on the model of Maziar.[1] In the spectral region below 1.7 eV the absorption depth for complete absorption is of the order 3-4 μm, while in the region above 1.7 eV, the absorption depth is of the order 0.3-0.4 μm. In order to significantly reduce the thickness of a GaAs cell it will be necessary to produce a reflector with high reflectivity in the spectral region from 1.4 eV to 1.7eV (890 to 730 nm).

Our approach is to achieve the epitaxial optical reflector by **growing a multilayer distributed Bragg reflector (DBR)** structure that has high reflectivity over the required spectral region. A Bragg reflector is a stack of alternating layers with a small difference in index of refraction. Such a stack can be constructed to have high reflectivity across a relatively wide spectral range if the layers are designed to be a quarter wavelength each near the desired wavelengths. A Bragg reflector constructed from two different compositions of AlGaAs could then be used, in principle, to construct the required reflector for GaAs or AlGaAs cells. The use of a periodically modulated refractive index to achieve high optical reflection is well established in the fabrication of conventional multilayer optical coatings. However, the fabrication of such reflectors using single crystal semiconductor layers has been investigated only recently as growth techniques have matured to achieve the required precision in composition and thickness. The lattice matched AlAs/GaAs system allows access to a continuous range of refractive index from 2.97 to 3.59 (at $\lambda=0.9$ μm). While this range is less than the refractive index difference in the dielectrics used in conventional optical coatings, high reflectivity can still be obtained in a semiconductor structure of modest thickness. The maximum reflectivity at λ_o is given by

$$R_{\max} = \left(\frac{1-n_{eff}}{1+n_{eff}}\right)^2 \quad where\ n_{eff} = \left(\frac{n_h}{n_l}\right)^{2N} \frac{n_s}{n_i} \qquad (3)$$

The s and i subscripts designate the substrate and incident media, respectively. It is apparent from inspection that the reflectivity increases not only with the number of pairs N in the reflector, but with the difference between the refractive indices of the two media. For the AlAs and $Al_{0.2}Ga_{0.8}As$ layers used in the EOR cell, the refractive indices

n at λ=840 nm are 2.990 and 3.452, respectively. There is a bandwidth associated with this reflectivity, and it is given by the relation

$$\Delta\lambda = \frac{4}{\pi}\sin^{-1}\left(\frac{n_h - n_l}{n_h + n_l}\right)\lambda_o \tag{4}$$

A simple analysis using the above relations indicates that when GaAs is considered the incident media, it will require approximately 13 periods to achieve 90% reflectivity for an $Al_{0.2}Ga_{0.8}As/AlAs$ DBR centered at 840 nm. The anticipated stop band is about 77 nm in width for a single reflector.

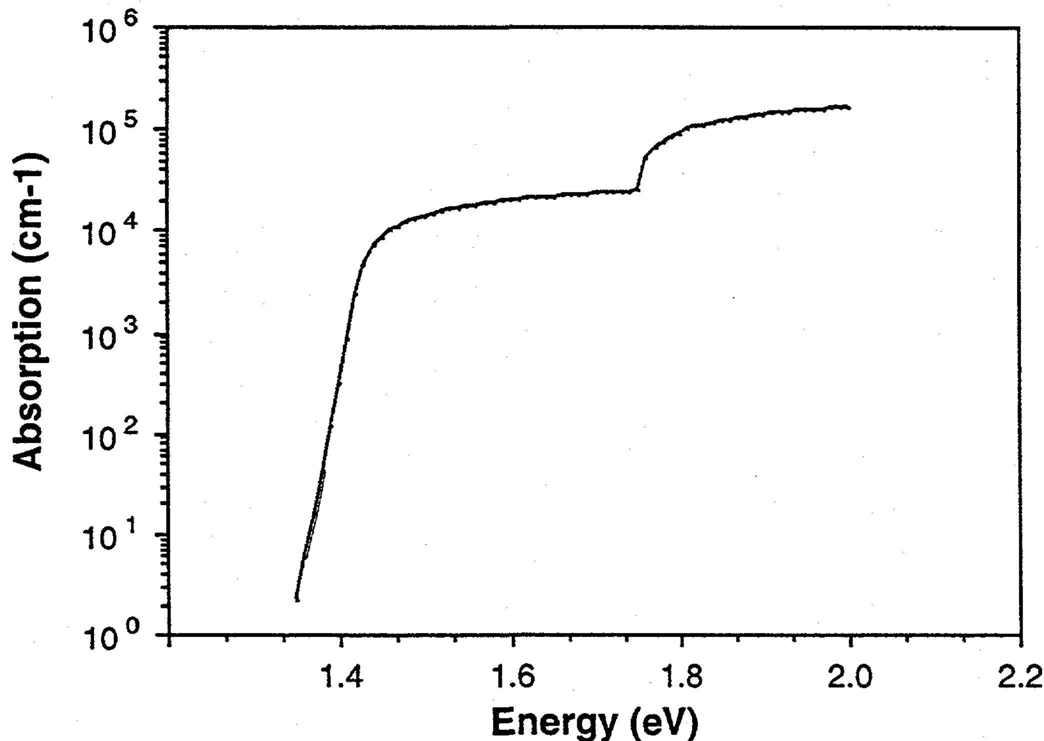

Fig. 5 Schematic absorption coefficient of GaAs vs. photon energy.

A wider bandgap, high reflectivity Bragg reflector could be realized with $AlAs/Al_xGa_{1-x}As$ by sequentially growing two reflectors tuned to different wavelengths. This situation can be described using a matrix approach describing the electric field propagation through the layers. For one reflector, a column vector representing the electric field components obeys

$$\begin{pmatrix} a_o \\ b_o \end{pmatrix} = \begin{pmatrix} A & B \\ C & D \end{pmatrix}\begin{pmatrix} a_N \\ b_N \end{pmatrix} \tag{5}$$

where a_o and b_o are the incident and reflected electric field components, respectively; a_N is the transmitted field, b_N is the field entering the back of the reflector (= 0 for single

reflector) and A, B, C and D are functions of the reflector parameters. The field reflectivity r_N and power reflectivity R are given by

$$r_N = \left(\frac{b_o}{a_o}\right)_{b_N=0} = \frac{C}{A} \tag{6}$$

$$R = |r_N|^2 \tag{7}$$

For two consecutive stacks of different composition (tuned to different wavelengths), the field at the end of both stacks is then related to the incident field by the product of their transfer matrices:

$$\begin{pmatrix} a_o \\ b_o \end{pmatrix} = \begin{pmatrix} A_1 & B_1 \\ C_1 & D_1 \end{pmatrix}\begin{pmatrix} A_2 & B_2 \\ C_2 & D_2 \end{pmatrix} \quad \begin{pmatrix} a_T \\ b_T \end{pmatrix} = \begin{pmatrix} A_T & B_T \\ C_T & D_T \end{pmatrix}\begin{pmatrix} a_T \\ b_T \end{pmatrix} \tag{8}$$

where 1 and 2 refer to the two quarter-wave stacks, respectively. Multiplying those matrices gives a composite matrix for the system, identified by the subscript T. The reflectivity of the pair of reflectors is then

$$r_T = \left(\frac{b_o}{a_0}\right)_{b_{N_1+N_2}=0} = \frac{C_T}{A_T} = \frac{C_1A_2 + D_1C_2}{A_1A_2 + B_1C_2} \tag{9}$$

Time reversal symmetry of the matrix elements reduces the expression to

$$r_T = \frac{C_1A_2 + A_1^*C_2}{A_1A_2 + C_1^*C_2} = \frac{r_{N_1} + r_{N_2}\left(\frac{A_1^*}{A_1}\right)}{1 + r_{N_1}r_{N_2}\left(\frac{A_1^*}{A_1}\right)} \tag{10}$$

where r_{N_1} and r_{N_2} are the field reflectivities of the individual reflectors. Consequently, the power reflectivity of the composite structure is

$$R_T = |r_T|^2 = \frac{{r_{N_1}}^2 + {r_{N_2}}^2 + 2\mathrm{Re}\left\{r_{N_1}^* r_{N_2}\left(A_1^*/A_1\right)\right\}}{1 + r_{N_1}^2 r_{N_2}^2 + 2\mathrm{Re}\left\{r_{N_1} r_{N_2}\left(C_1^*/C_1\right)\right\}} \tag{11}$$

It is evident that two reflectors whose spectra do not have high reflectance in the same wavelength regions will result in a reflectivity spectrum that is nearly the sum of the two individual spectra, that is $R_T = R_1 + R_2$ if $r_{N_1}r_{N_2} << 1$. Fig.6 shows the calculated reflectivity spectrum of two Bragg reflectors tuned to 750 nm and 820 nm. Each reflector has 30 periods of $AlAs/Al_xGa_{1-x}As$ with x=0.3 and 0.2 for the

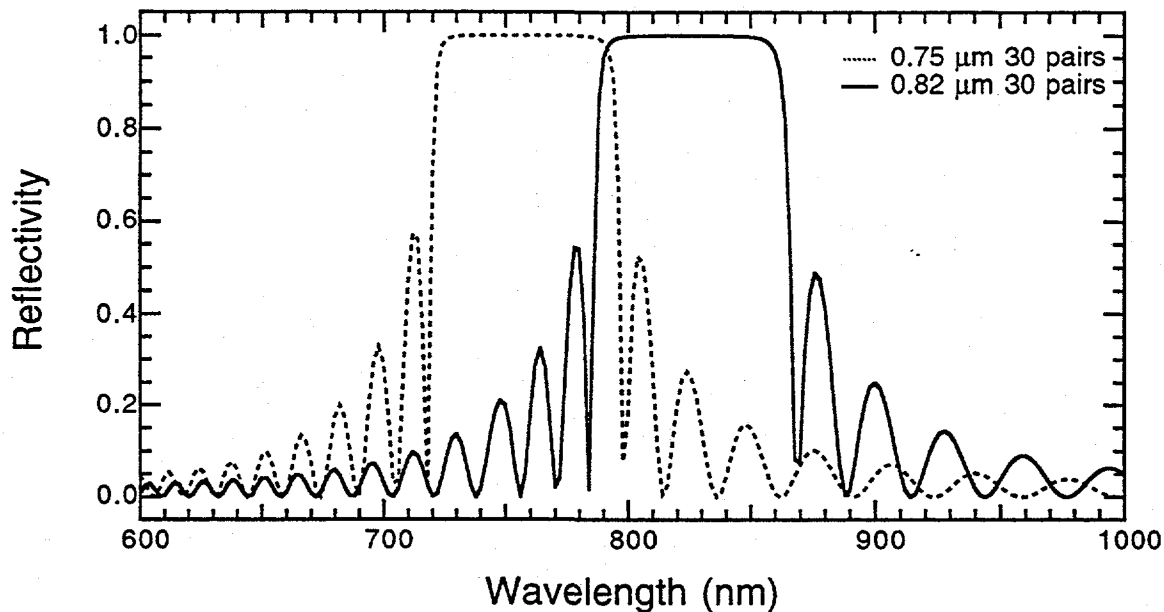

Fig. 6 Calculated reflectivity of two component reflectors with 30 periods of 750 and 820 nm, respectively.

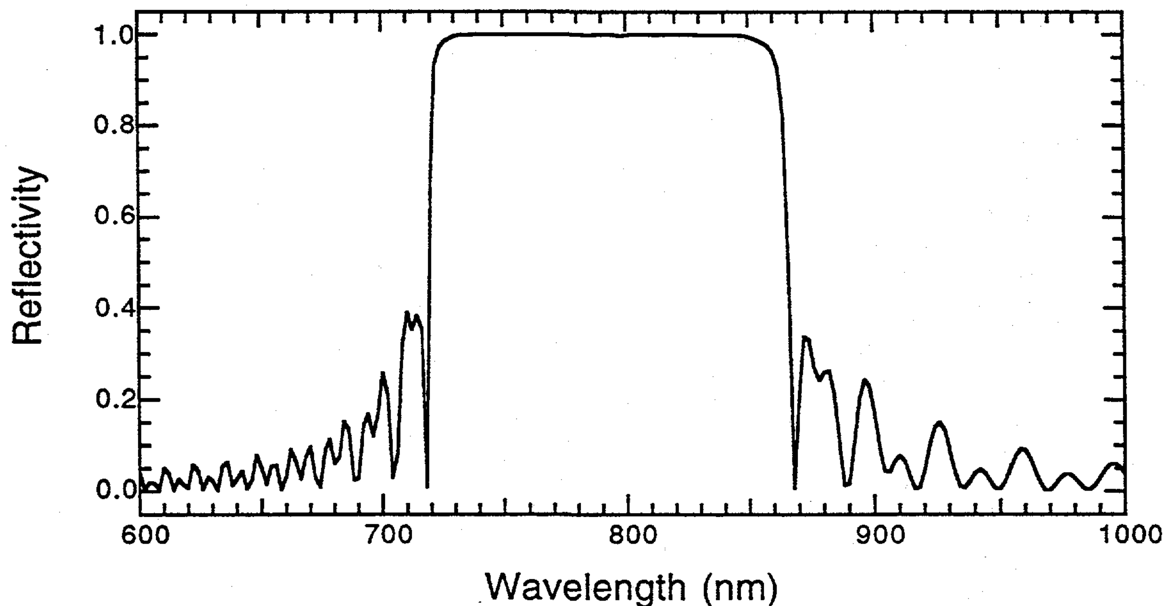

Fig. 7 Calculated reflectivity of a composite Bragg reflector using the component reflectors of Fig.6.

short and long wavelength reflectors, respectively. Note that the reflectivity of each approaches unity over a wide spectral range when this number of periods is assumed. Fig. 7 shows the composite reflectivity that would result if these reflectors were grown on top of one another. Note that the spectral region of high reflectivity for the composite corresponds to the sum of the bandwidths of the component reflectors.

The reflectivity spectra shown above were calculated without accounting for the effects of absorption. The program developed at USC to calculate the reflectivities of multistack mirrors was modified to consider several different models of absorption. The effects of absorbtion on the reflectivity response is seen primarily at shorter wavelengths as a softening of the short wavelength shoulder of the stop band, and in the suppression of satellite peaks below the stop band. The overall bandwidth of reflectivity is also slightly reduced. Shown in Fig. 8 is a recalculation of the reflector design shown in Fig. 7, but with absorption effects included. The absorption data used in this case was measured by Aspnes et al.[2] Note that the edges of the stop band are less distinct, especially at shorter wavelengths. In addition, the stop band is not flat, but contains some features. The large dip in the center is due to a slight narrowing of the stop band of each reflector, which in turn causes the separation between the stop band centers to be larger than the stop band widths themselves.

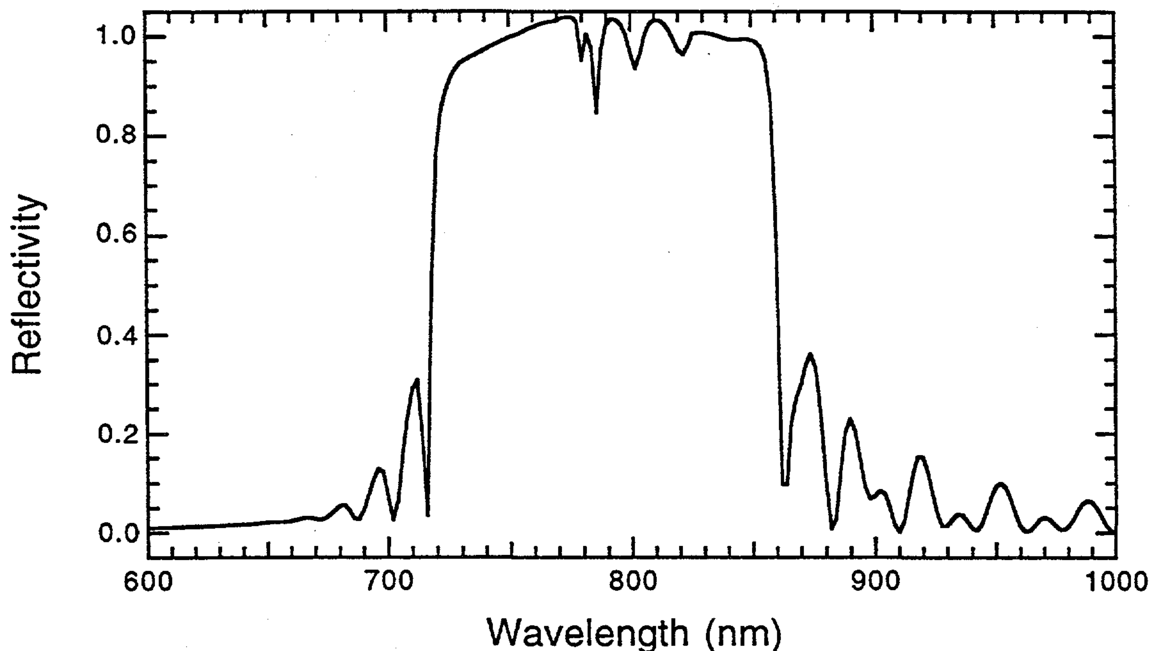

Fig. 8 Calculated reflectivity of composite reflector shown in Fig. 7, but with absorption considered.

In Fig. 9 the effect of reducing the number of periods in half is demonstrated by comparing the reflectivity of composite reflectors with 15 and 30 periods. Note that the thinner (15 pair) reflector maintains a high reflectivity over much of the bandwidth of the 30 period reflector. The abruptness of the rise and fall of the reflectivity is reduced however for the thinner reflector.

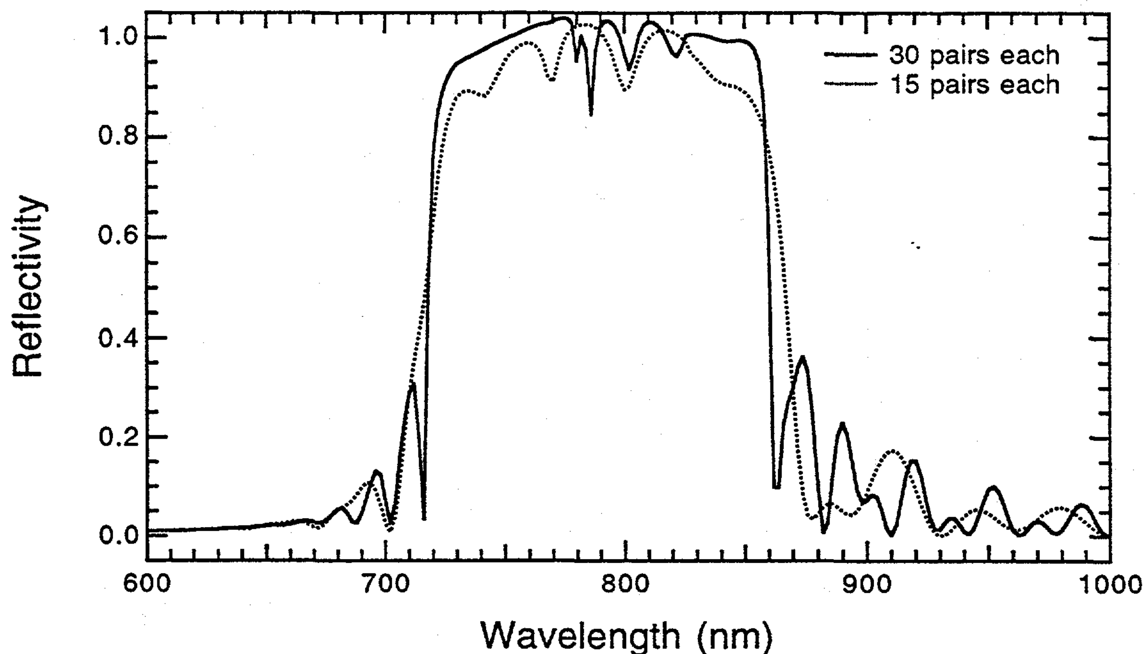

Fig. 9 Calculated reflectivity of twin Bragg reflectors containing fifteen and thirty periods. Absorption effects are included.

From this analysis, a two reflector stack appears sufficient to satisfy the requirements for a GaAs solar cell.

The goal of the reflector design is to achieve R>0.90 in the spectral region from 720 nm to 860 nm - the wavelength regions in which GaAs has an absorption coefficient less than 10^4 cm^{-1}. Prior to the start of the program we had shown that the total reflectivity of stacked reflectors composed of multiple period Bragg reflectors is rigorously predicted by the superposition of the reflectivities of the individual reflector components. Thus, one can construct a wide band reflector by stacking reflectors with different center wavelengths. Near unity reflectivity is predicted over the desired range by the use of two reflectors, each thirty periods thick, with the appropriate center wavelengths. Unfortunately, the use of such a composite results in a reflector nearly 6 μm thick. An optimization analysis was performed with the goal of minimizing the total epitaxial thickness of the reflectivity stack while maintaining the desired reflectivity.

We have chosen an Al composition of 0.2 for all of these data so that the reflector will be transparent to all wavelengths of interest. This choice is based upon the present knowledge of the energy gaps and the index of refraction for this material. This composition material also forms a significant electron/hole reflecting barrier. We used only one composition of AlGaAs to avoid complicating the growth of the structure. The calculated reflectivity spectrum of the three designs listed below is shown in Figs. 10-12:

Table 1- Epitaxial Reflector Designs

Epitaxial Optical Reflector Design #1

15.5	pairs	$Al_{0.2}Ga_{0.8}As$ / AlAs	628Å / 722Å
13	pairs	$Al_{0.2}Ga_{0.8}As$ / AlAs	583Å / 672Å
9	pairs	$Al_{0.2}Ga_{0.8}As$ / AlAs	545Å / 632Å
6	pairs	$Al_{0.2}Ga_{0.8}As$ / AlAs	529Å / 614Å

Total Thickness 5.47 µm

Epitaxial Optical Reflector Design #2

8 .5	pairs	$Al_{0.2}Ga_{0.8}As$ / AlAs	625Å / 721Å
8	pairs	$Al_{0.2}Ga_{0.8}As$ / AlAs	600Å / 693Å
8	pairs	$Al_{0.2}Ga_{0.8}As$ / AlAs	566Å / 656Å
8	pairs	$Al_{0.2}Ga_{0.8}As$ / AlAs	541Å / 628Å

Total Thickness 4.09 µm

Epitaxial Optical Reflector Design #7.1

25.5	pairs	$Al_{0.2}Ga_{0.8}As$ / AlAs	613Å / 707Å
25	pairs	$Al_{0.2}Ga_{0.8}As$ / AlAs	549Å / 638Å

Total Thickness 6.334 µm

The conclusions we have reached from our modelling is that the wavelengths near the bandedge of GaAs with the longest wavelength and lowest absorption coefficient require the highest reflectance and thus the most periods. This sets some lower limit on how thin the reflector can be. A properly designed reflector with a total thickness of 4.1 µm appears to be adequate as a back reflector.

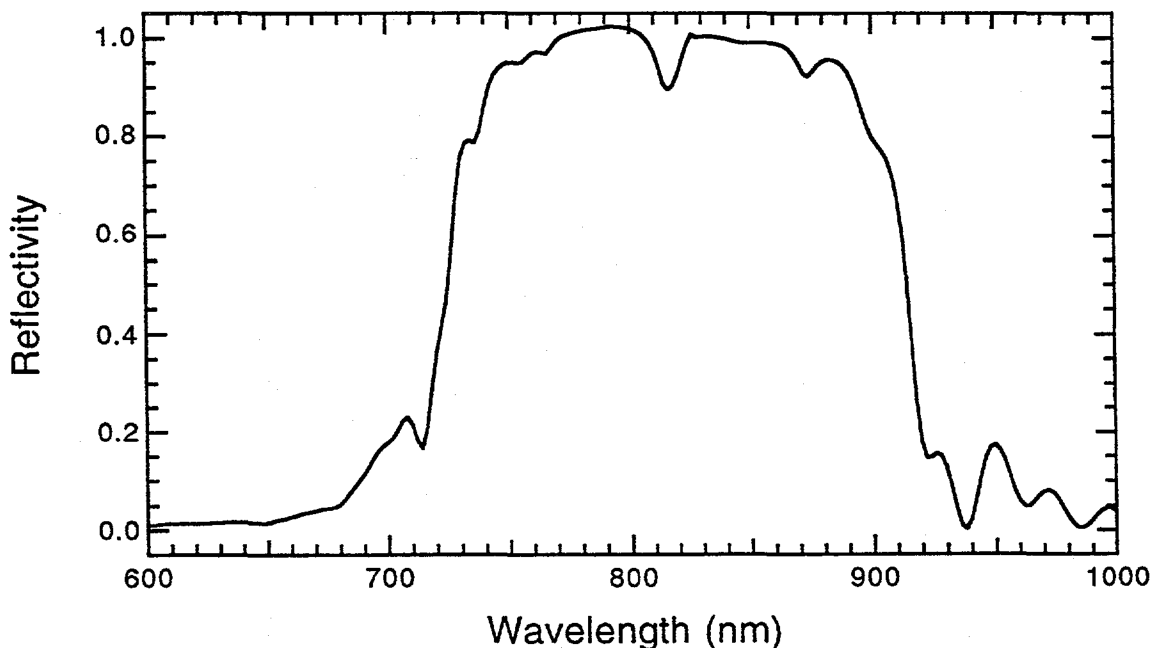

Fig. 10 Calculated reflectivity of design #1 (with absorption)

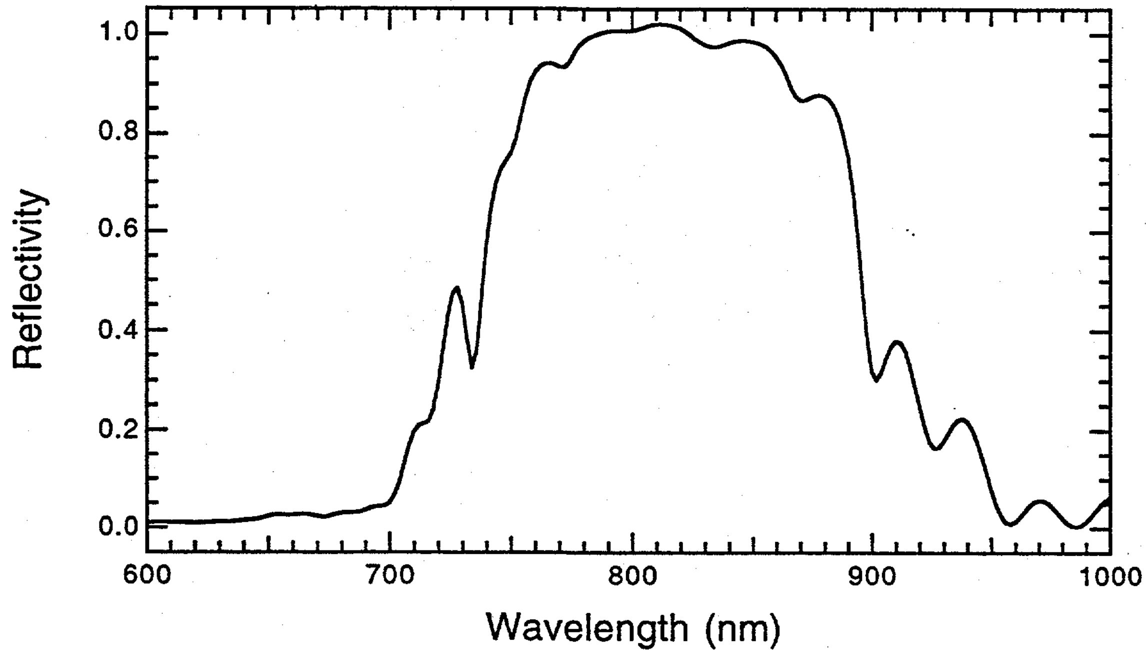

Fig 11 Calculated reflectivity of design #2 (with absorption)

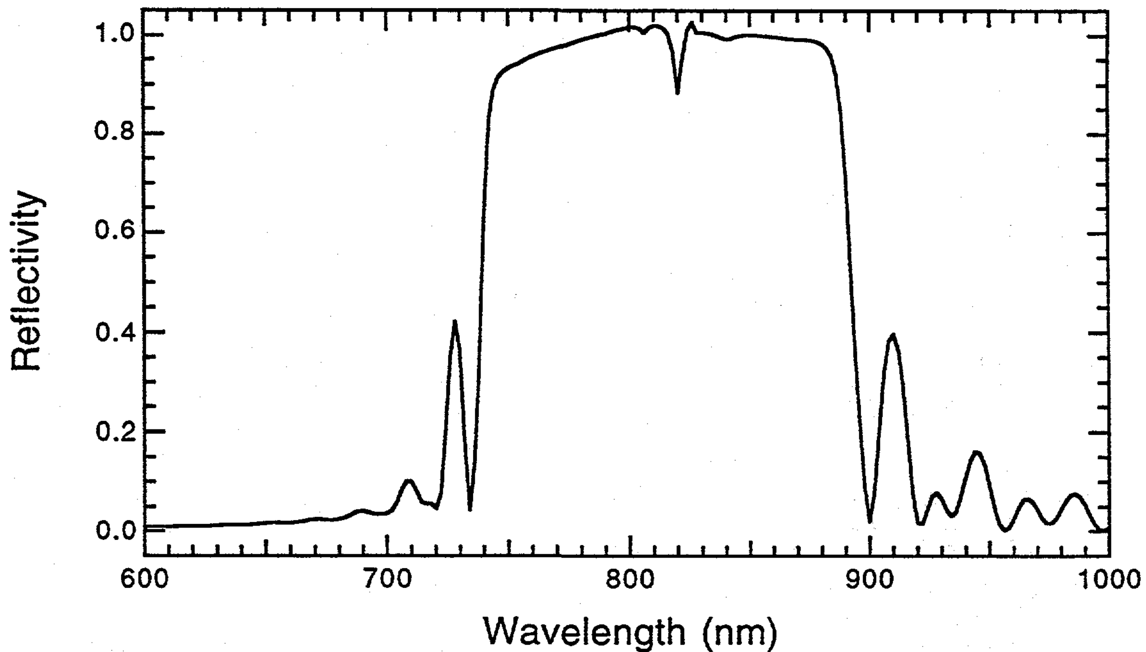

Fig. 12 Calculated reflectivity of design #7.1 (with absorption)

The DBR simulation program developted at USC was also used to study the effects of number of periods, layer thickness and composition change on the optical response. Results were obtained on reflectors centered at both 0.98 μm and 0.84 μm, but only the latter will be presented here. For the EOR solar cell, preliminary numerical results suggest that a reflectance of only 90% is necessary to achieve the desired result. This is

certainly an advantage, since limiting the number of epitaxial layers reduces the complexity of the device. The first task for the simulation routine was to center the reflectors such that greater than 90% reflectivity is available for the most critical range in the device, which is at and just above the bandgap of the GaAs absorbing region. The width of the stop band was calculated to be approximately 77 nm for a single band, indicating a properly positioned mirror should be centered at approximately 0.84-0.85 µm. Shown in Fig. 13 below are three 25 pair DBRs calculated without absorption effects at varying centers of reflection relative to the GaAs band edge.

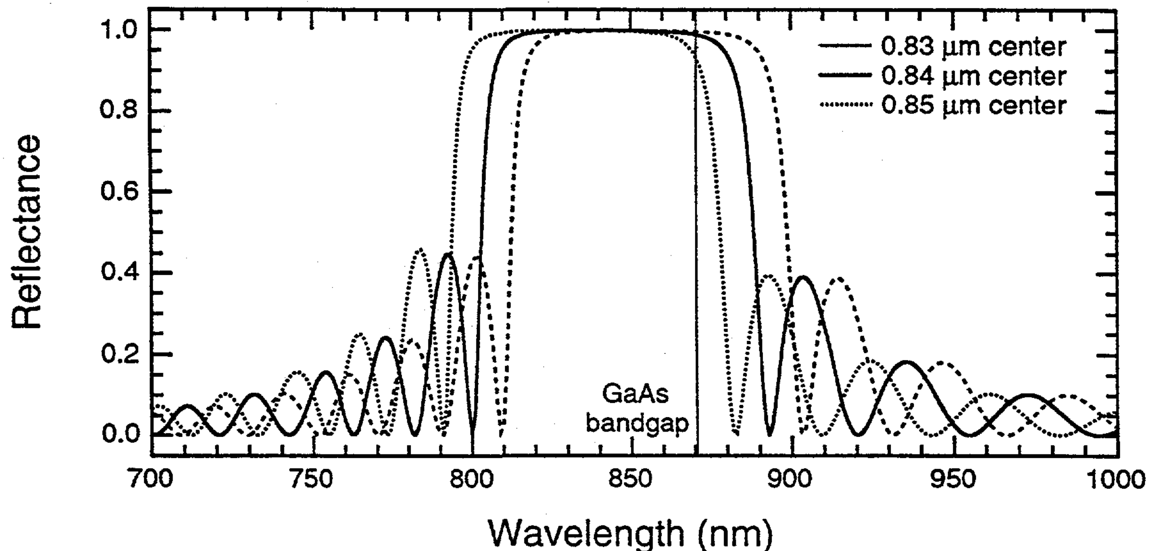

Fig. 13 Reflectance vs. wavelength for DBRs centered at 0.83, 0.84, and 0.85 µm. Notice the position of the high reflectance region relative to the GaAs bandgap.

It is demonstrated in this graph that a center wavelength of 0.84 µm is appropriate for DBRs composed of 25 periods.

The optical response of DBRs is very sensitive to layer thickness. The variation in thickness of the epitaxial layers grown by MOCVD can vary several percent from run to run, as well as across the wafer itself. Several cases were considered and calculated, but the trend is properly illustrated in the Fig. 14. This case considered the designed layer thicknesses of 702Å for AlAs, and 608 Å for $Al_{0.2}Ga_{0.8}As$ to have both varied by 1% in the same direction. This amounts to about a 6 Å change in thickness, or approximately 0.35 seconds at the growth rates generally used for these structures. The change in the thicknesses of both layers resulted in a stop band movement of about 8 nm.

Although not shown, simulations of the same structure where only one of the layers was changed showed a change in the stop band position of 4 nm. This indicates that the movements off of the designed center wavelength resulting from thickness can be summed together, at least across the small range of thickness errors considered here.

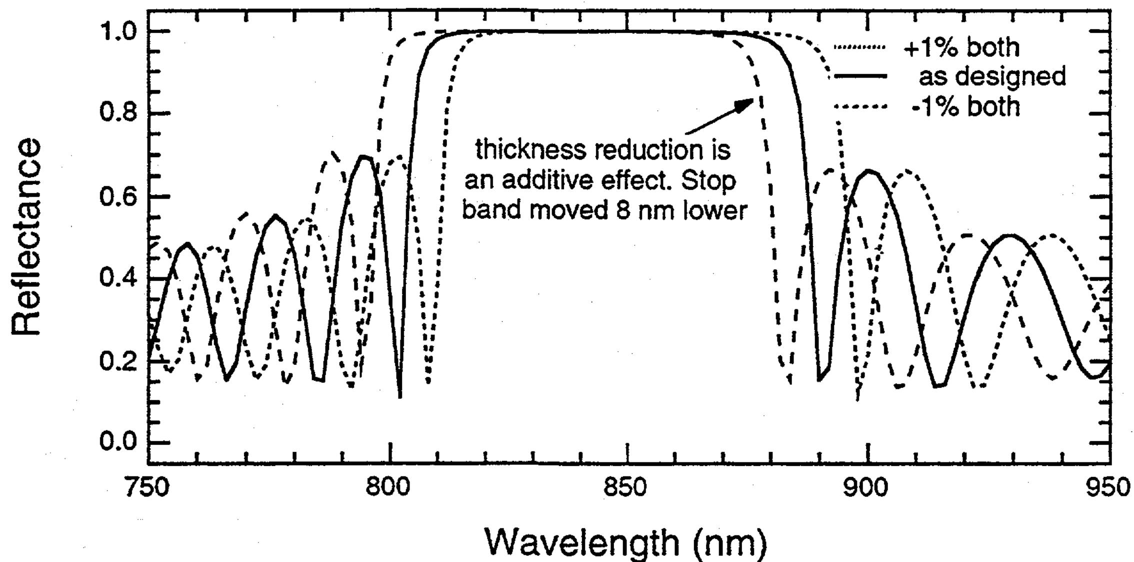

Fig. 14 Reflectivity curves for 25 period DBRs exhibiting thickness changes in both layer media of ±1%.

When one layer was increased, and the other reduced 1%, the errors approximately cancelled. All of these possible combinations of change are realistically possible variations which can occur in the MOCVD growth process.

Variations in source fluxes can also lead to changes in alloy composition. Differences between expected and measured AlGaAs compositions have been measured as high as 3% in our laboratory. Fig. 15 summarizes the effect of composition on stop band position.

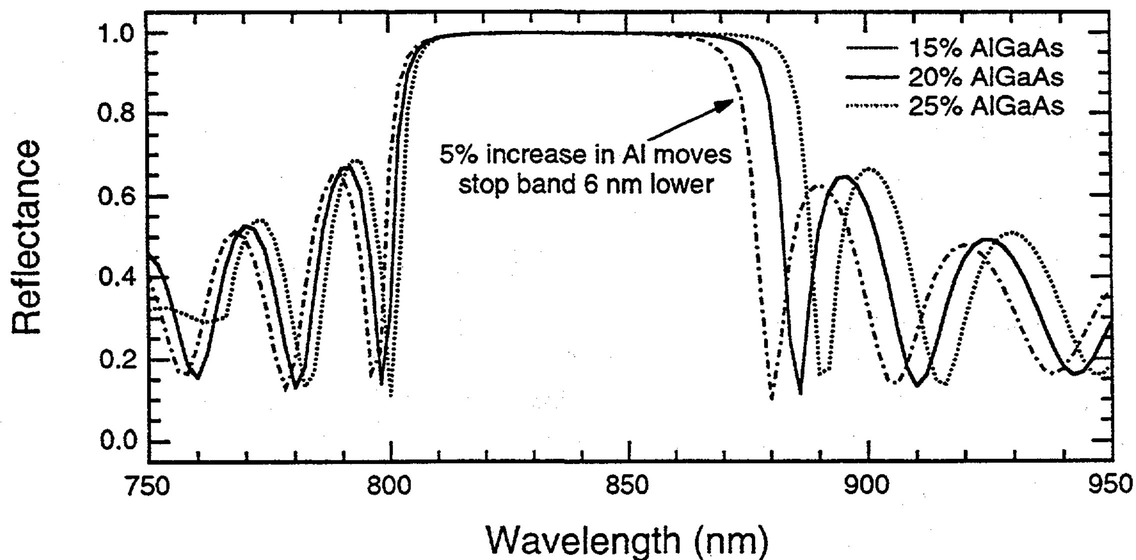

Fig. 15 The effect of an error in alloy composition on the optical response.

For a relatively large change in alloy composition of 5%, the stop band has moved approximately 6 nm (assuming the thicknesses have not changed). What is also elucidated by this result is that an increase in composition from the designed level is a more serious problem than a reduction in composition. The long wavelength edge of the stop band, near the GaAs absorption edge, moves much more than the shorter wavelength edge. An increase in composition may move the stop band edge below the point where absorption becomes substantial. The non-reflected photons would have long optical absorption lengths and may not be collected by the cell.

Modelling of solar cell performance was undertaken during the early stages of this project in collaboration with Martin Klausmeier-Brown at Varian by using Varian's CELLOPT program and PC-1D (Paul Basore). Fig. 12 shows the cell design used in these initial studies. Sensitivity to n on p vs p on n designs has been investigated and the initial conclusion is that p on n will be most suitable. To determine the effect of the reflector on cell performance, we first show in Fig. 17 the dependence of cell efficiency on base layer thickness for a conventional cell with no optical reflector (Fig. 16). Note that the base thickness must be of the order of 2.5 - 3.0 μm to achieve the optimum efficiency. This agrees with our initial back of the envelope estimate.

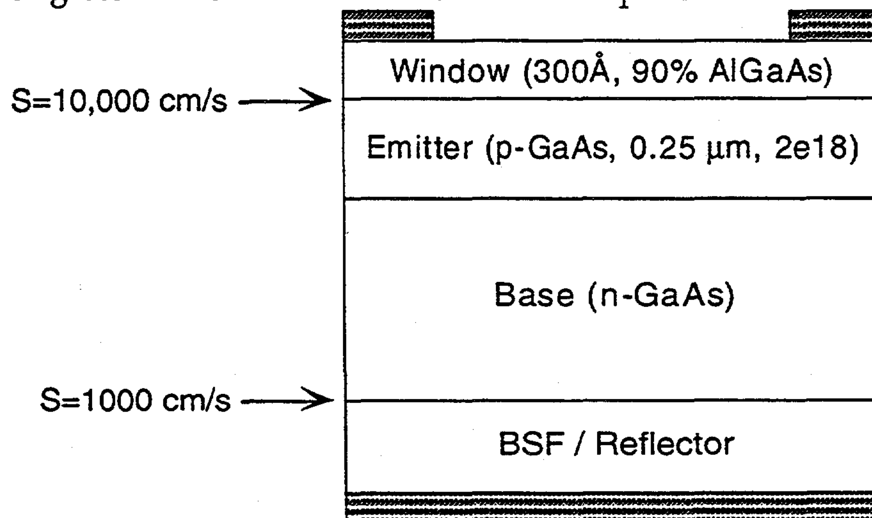

Fig. 16 Epitaxial structure used in cell modelling by Klausmeier-Brown

The incorporation of back surface optical reflections is difficult in CELLOPT. As a result PC-1D was initially modified to include this difference. The back optical reflectance is entered as a singular value, and as such, can not be varied with wavelength. This feature therefore approximates, but does not accurately represent the optical response of a DBR structure. Using a back optical reflectance of unity PC-1D predicts an efficiency of 24.2% for 1-sun AM0 for a base width of only 1 μm.

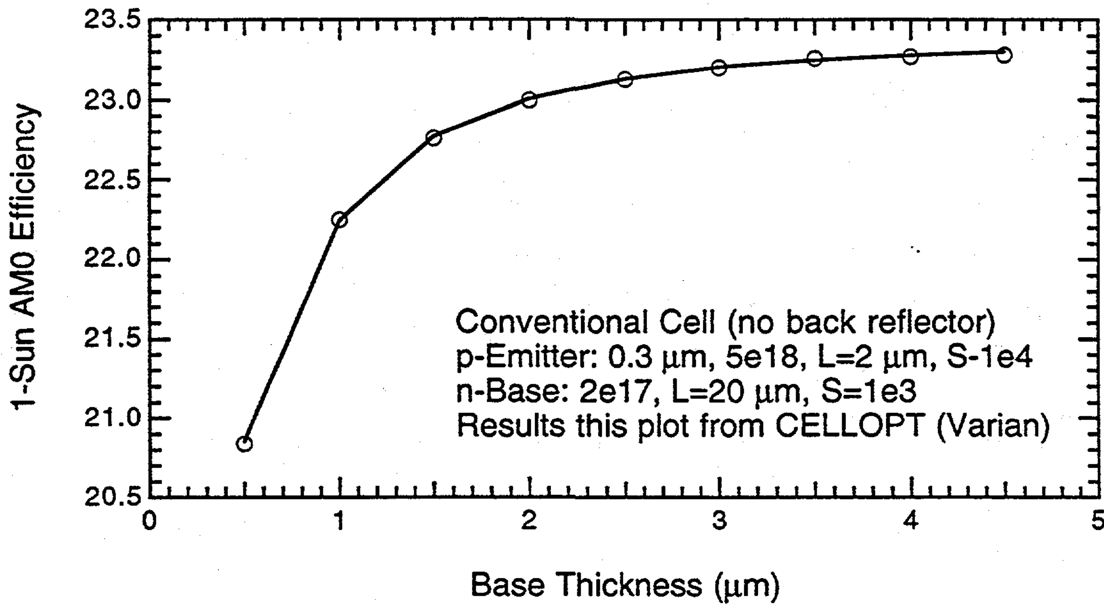

Fig. 17 Dependence of cell efficiency on base thickness

Fig. 18 shows the quantum efficiency of that cell using a conventional 1 layer anti-reflection coating. The achievement of unity optical reflection will require excessive epitaxial optical thicknesses, as indicated in the previous section. PC-1D predicts that the efficiency of the optimal cell will decrease to 24.1% for R=.999.

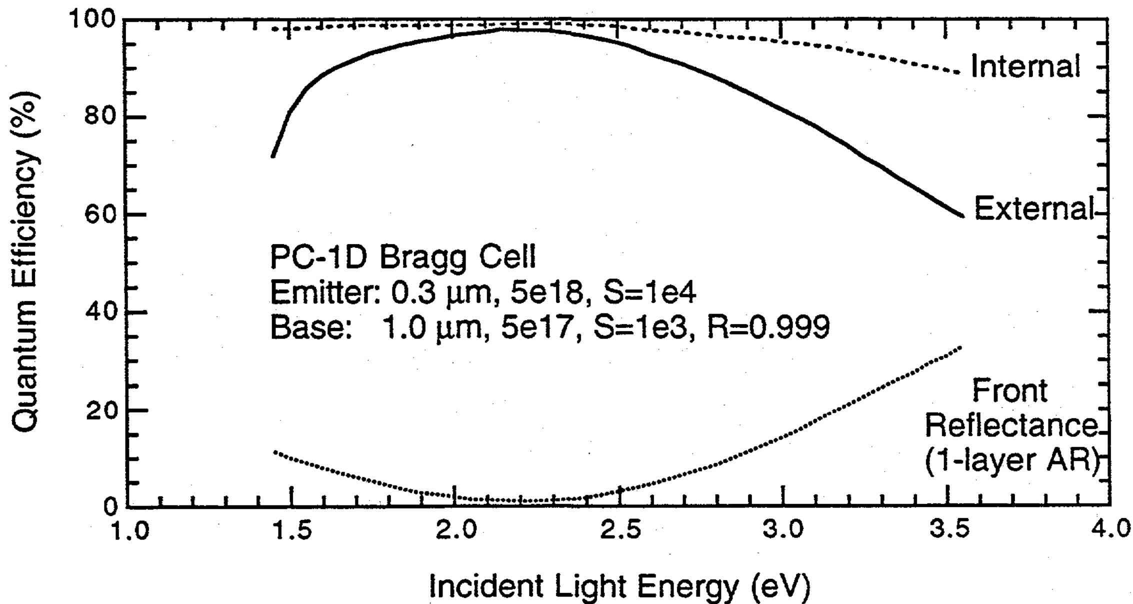

Fig. 18 Quantum efficiency of a cell using a back surface optical reflection

The most important issue in the design of the cell is to insure that all of the photogenerated carriers can be captured. To determine this we have carried out some modelling of the spectral response of EOR cells using PUPHS. Specifically, we have

investigated the effect of reducing the cell thickness on the spectral response of the solar cell to confirm the efficacy of the epitaxial optical reflector. We choose to model a P-p-n-N heteroface solar cell. The emitter thickness was arbitrarily chosen to be 0.25 µm and the base was chosen to be 2.0 µm for non-EOR cells, and 1.0 µm for EOR cells. In Fig. 19 the quantum efficiency of three cells is shown, with the only differences being the structure of the layer underlying the base layer, and the thickness of the base layer itself. Note that the presence of a $Al_{0.3}Ga_{0.7}As$ layer slightly enhances the collection of photons with energy greater than 750 nm. Photon collection in the same wavelength range is greatly enhanced in the EOR cell, even though the base layer is half as thick.

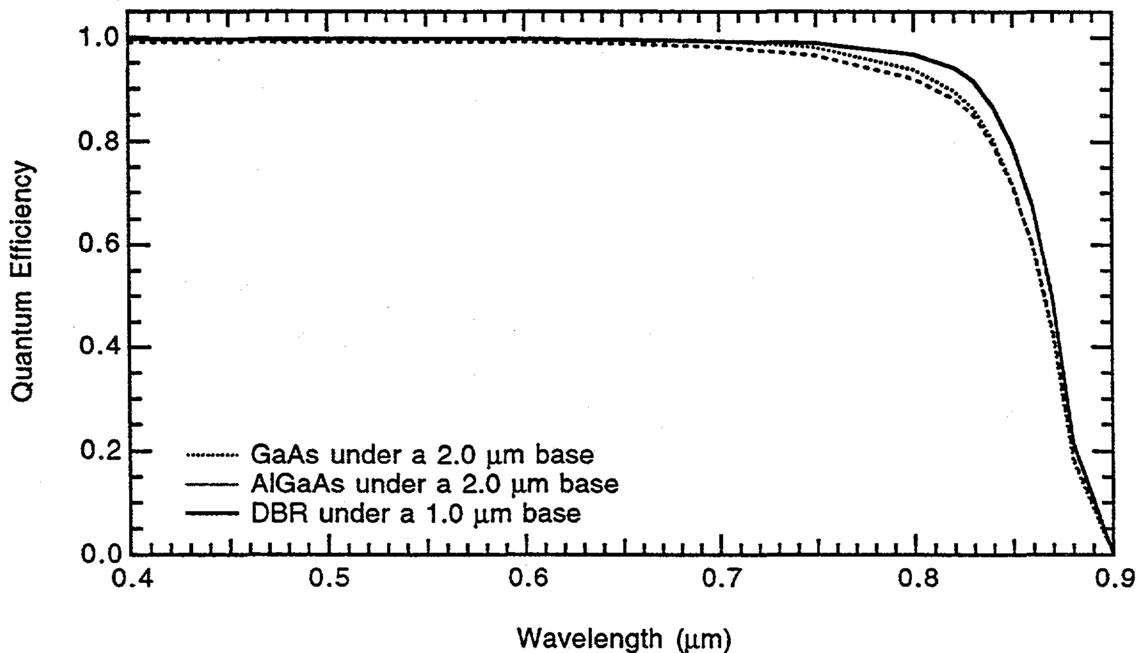

Fig. 19 A comparison of similar cell designs with varying back surface structures

The EOR cell structure decreases the sensitivity to base doping and lifetime parameters due to this enhanced collection of photons near the bandgap of GaAs. In Fig. 20 we plot the spectral responses for devices that differ by an order of magnitude (10^{16} vs. 10^{17}) in doping and lifetime (50 ns vs. 5 ns). Neither the width of the space-charge region or the magnitude of the diffusion length play a major role in the carrier collection for this structure limited device.

The modification of CELLOPT to include a rear optical reflector was carrier out by Klausmeier-Brown and the optimum efficiency was calculated as a function of doping of the base layer. The data are shown in Fig. 20 for the case of 1-sun AM0 conditions before and after irradiation with 1 MeV electrons. The first conclusion that this modelling suggests is that total active thicknesses in the range 1.3 - 1.5 µm can produce

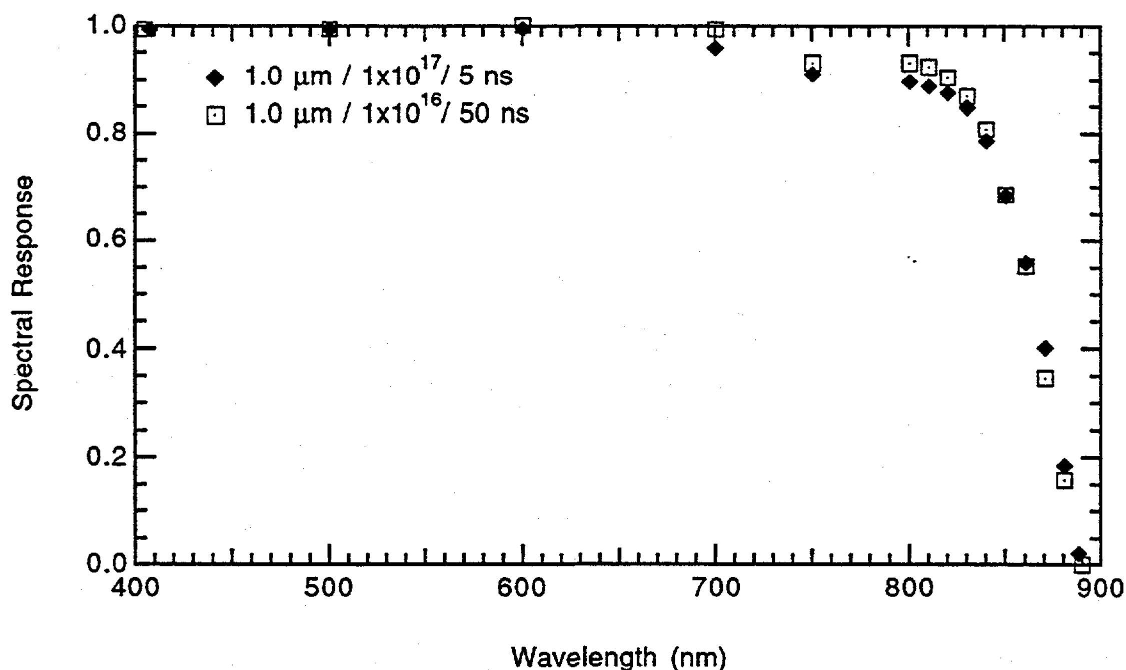

Fig. 20 Calculated spectral responses for EOR cells with 1.0 μm bases and different doping and lifetime values.

high efficiencies in the EOR cell. If adequate diffusion lengths can be achieved in heavily doped material, this thickness would promote much higher open circuit voltage and higher efficiency at the loss of a small amount of photocurrent. The second conclusion reached is that our assumption that R_b~0.90 is adequate for the EOR cell is confirmed, since the differences in the cell efficiencies for the case of R_b=1.0 and R_b=0.9 are shown to be minimal. The effects of radiation on the efficiency are a matter of only peripheral interest in this program but the calculations suggest that the EOR cell has a substantially reduced rate of damage and degradation as compared to a conventional cell.

Of major interest to this program is the effect of the EOR design on the efficiency of concentrator cells. Based upon CELLOPT parameters there was little difference between the n on p and p on n structures and similar conclusions with respect to insensitivity of efficiency upon cell parameters prevails for both designs. The efficiency of n on p concentrator cells under 1000 sun AM1.5 conditions shown in Fig. 21 shows that EOR cells have higher efficiency than conventional cells over the range of reasonable base dopings. This higher efficiency together with the reduced sensitivity to degradation predicted by the data of Fig. 20 suggest that the EOR cell has considerable promise as an efficient terrestrial cell. The calculations summarized above provided sufficient direction to motivate the experimental work.

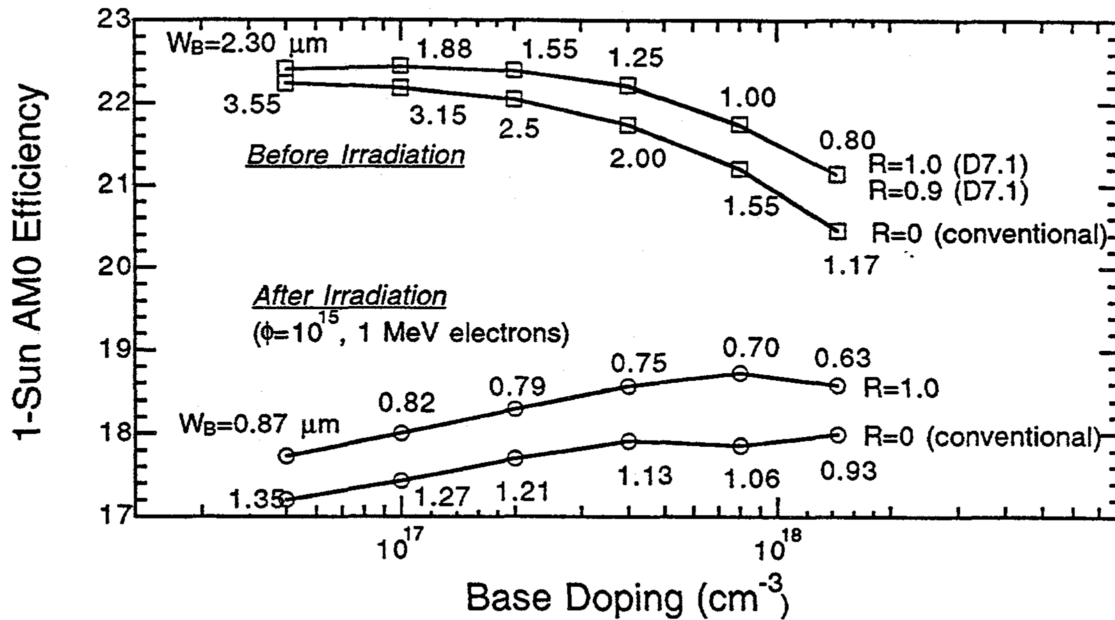

Fig. 20 A comparison of conventional and EOR solar cell efficiency before and after exposure to radiation

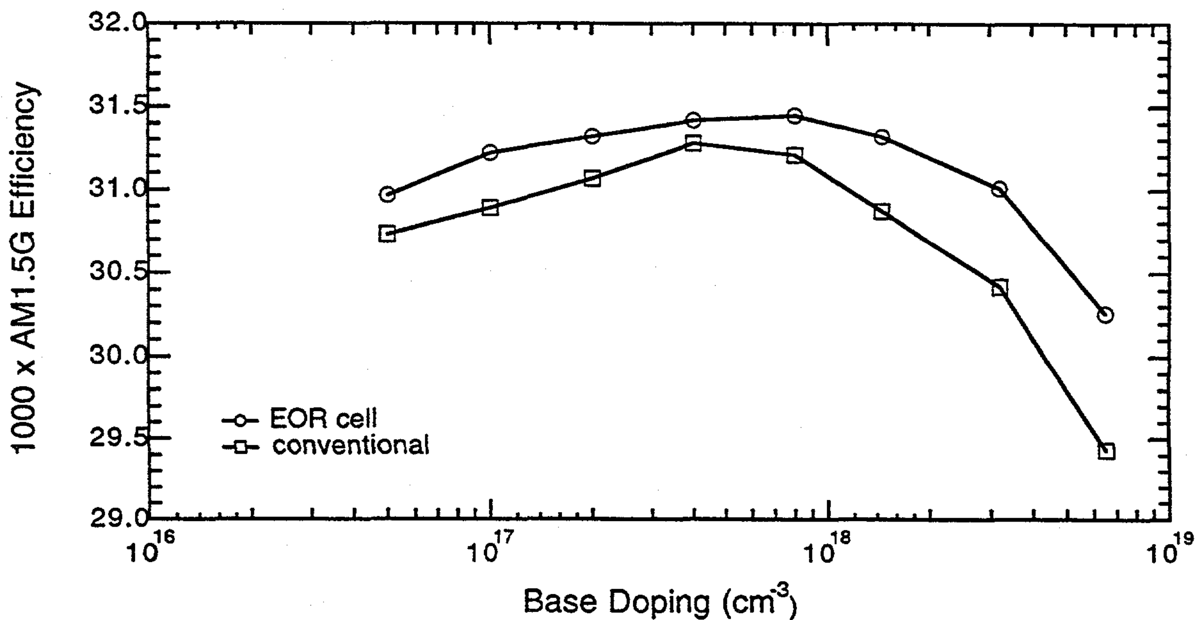

Fig. 21 A comparison of conventional and EOR solar cells under 1000 suns illumination

The simulation packages used by both Klausmeier-Brown and USC (CELLOPT, PC-1D, PUPHS) are capable of incorporating the effect of a back surface reflector only as a single reflectivity value maintained over all wavelengths. This is adequate for initial investigations, but it was felt that a more accurate description would be desirable for further study. Towards this end, in July 1992 USC obtained a new commercial available

two-dimensional semiconductor device simulator called Semicad Device. It was developed by Dawn Technologies of Sunnyvale, CA. Semicad Device is a sophisticated and versatile package with access to its feature set provided by a C-like programming language. The key feature of importance to this project is the ability to describe any interface or surface with reflection behavior that varies with wavelength.

The first five months of development with this new product were hampered by the learning curve associated with an advanced software application, in addition to several key software bugs uncovered by USC which prevented a converged solution under illuminated conditions. These problems were corrected by Dawn in a release obtained in December. Some initial solar cell device results were obtained shortly after. Although development of accurate material models and subsequent investigation of the desired parameter space are continuing, it is too early in this work to report any of the results obtained from Semicad Device. This work will continue beyond this project.

Task 2 - Materials Growth and Optimization

Prior to the start of this program and since its inception we have undertaken the growth of Bragg reflectors to establish that growth rate stability and control is adequate to growth the reflectors required for this program reproducibly. To test this we have grown reflectors using the binary pairs of AlAs/GaAs. We choose the center wavelength of these reflectors to be at wavelengths longer than the absorption edge of GaAs (0.98 μm) to allow us to characterize them without the influence of absorption. Our results show that the growth rate during a run is stable enough to be able to grow reflectors with R~1.0 for 30 period reflectors. However, we immediately observed that the reproducibility of the Bragg reflectors was less than adequate. The center wavelength of the reflectors varied by more than ± 6%. For a Bragg reflector centered at 0.85 μm, this level of variation leads to a ±0.051 μm variation of the center wavelength and a concomitant change in the edges of the reflectivity band. An extreme example of the variations that we have observed from run to run are shown in Fig. 22. These spectra are not corrected for the reflectance variation of the standard, which accounts for the variation in peak height. It is obvious that the center to center variation will create reproducibility problems when one tries to grow very high efficiency cells.

A schematic drawing of our reactor vessel and reactor manifold design are shown in Fig. 23. The vessel is a vertical design with a baffle at the top added specifically to create turbulence and improve mixing. The manifold is a conventional vent-run manifold with the switching manifold near the inlet to the reactor. All epitaxial growth runs are performed under atmospheric pressure conditions.

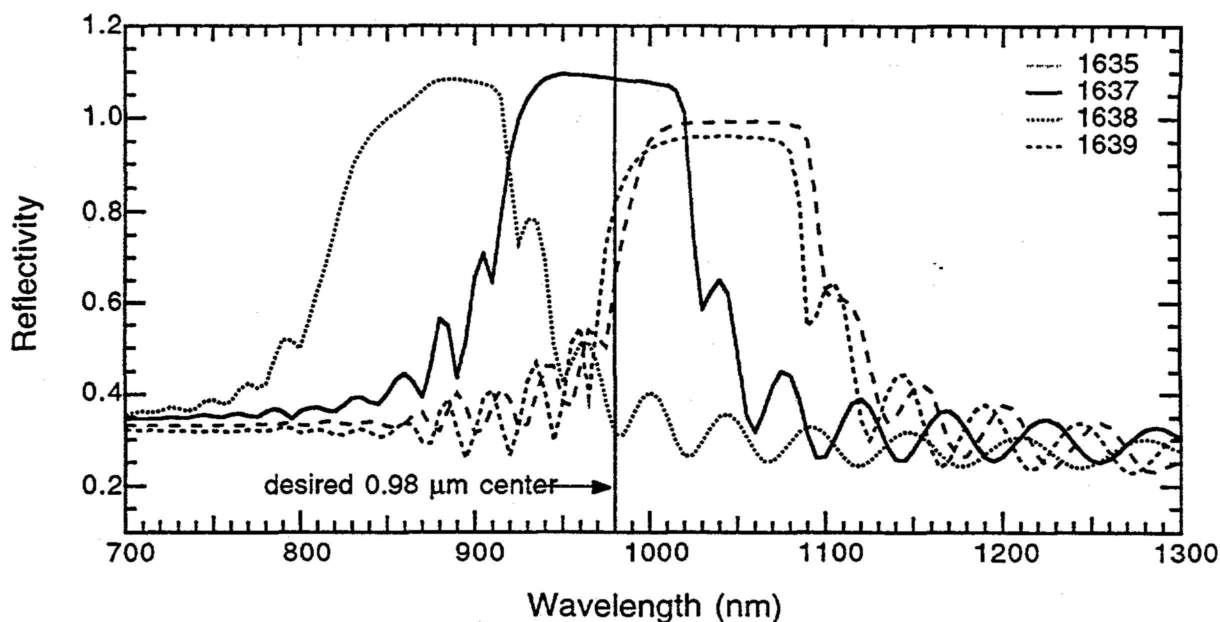

Fig. 22 Run to run variations of DBR reflectivity center

The reactor was shut down for six weeks during August and September of 1991 for a major modification. An additional reactant manifold was added to the system to accommodate a second Al source, an In source, a second Ga source and an alternate As source. All of these modifications benefited this program. The second Al and Ga sources are required for the growth of reproducible AlGaAs/AlAs Bragg reflectors. Prior to this modification, the reactor had only one of each source, requiring a change of the flow rates between each layer or an excessively long growth time. With the addition of new sources the flows for each of the Bragg layers can be set up prior to the growth and merely switched into the reactor. The reduced overall growth time improved overall reproducibility.

An intensive study of the possible causes of growth rate variations that led to Bragg reflector positioning difficulties was undertaken. The variations we see are a direct result of a variation in the growth rate since in the data of Fig. 22 we are dealing only with binary reflectors, and there can be no contribution from compositional variations. The growth rate, to first order, is a linear function of the concentration of organometallic group III components in the gas phase. There is a minor dependence on hydrodynamic variables in our reactor. The group III concentration, in turn, is dependent on temperature of the group III bubbler and the flow rate through the bubbler. Also, the growth of thin layers can be affected by transients in the switching of the gasses into the reactor. We have investigated each of these issues.

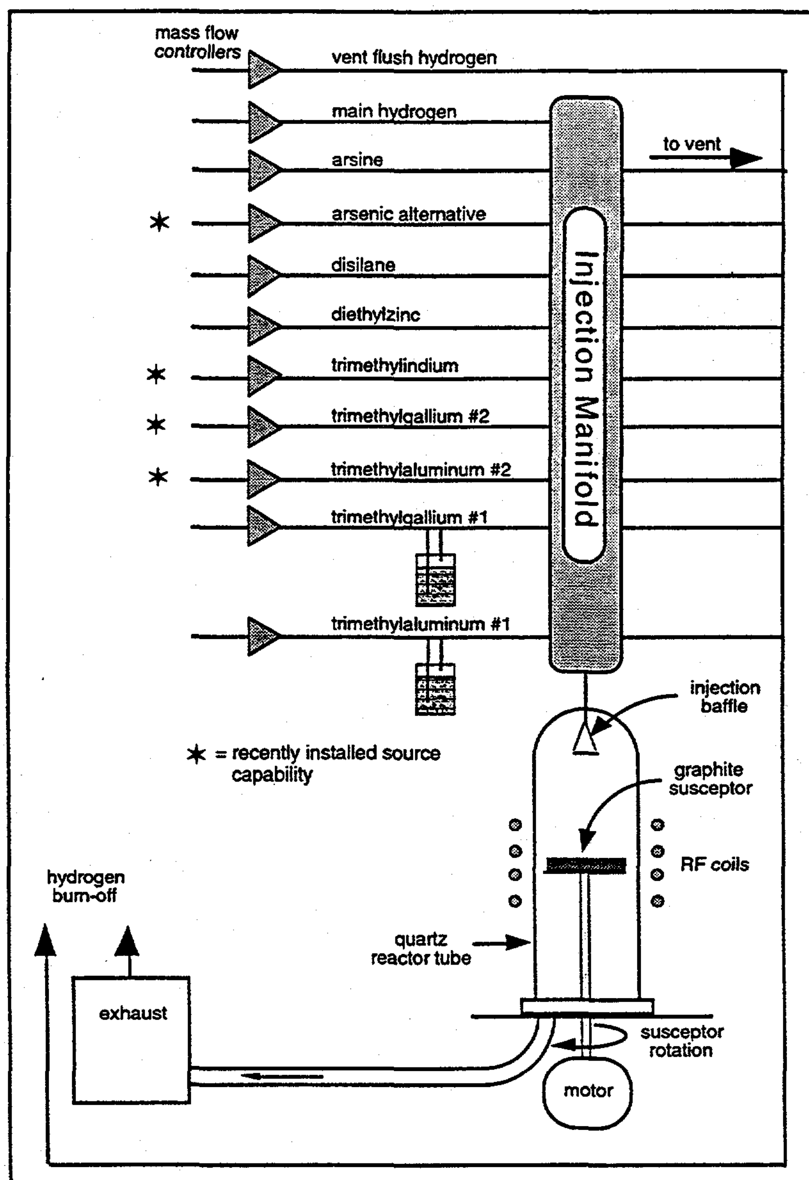

Fig. 23 A schematic drawing of the MOCVD reactor

The temperature of the baths in which our bubblers sit, particularly trimethylgallium, were found to vary by a 2-3 °C even though the bath is a static ice bath. Poor reproducibility in the distribution of the ice in the water was found to be the cause. As a result the growth rate could vary by as much as 20%. The bubblers were placed in actively cooled baths to alleviate this problem. This does not fully eliminate potential problems, since the limit of temperature control in these baths is ±0.1°C, which can still have an adverse affect on growth rate reproducibility.

We also found a correlation between the growth rate and the reactor back pressure caused by variations in the impedance of our reactor output filter. This resulted in our modifying the output to minimize the variation with time as the filter is used. Relatively

small changes 0.5 Torr - 1.0 Torr were sufficient to cause significant changes in growth rate. Finally by attaching a readout to all of our mass flow controllers to monitor their flows before and after switching of the injection manifold, we observed a switching transient in the flows that has an unknown effect on growth rate. This transient occurred in the absence of any obvious fluctuations in the differential pressure between the inlet to the reactor and the vent line. We modified the manifold to minimize these transients. We also increased the diameter of our output vent line on the manifold to eliminate clogging that can occur during long growth runs with high aluminum flows. In spite of all of these changes we continued to observe unacceptable growth rate changes. This forced us to conclude that an in-situ monitor of some kind was necessary to measure and possibly control the growth rate.

Laser Interferometry as Applied to In-situ Monitoring

To effect an in-situ monitor of the growth rate we have focused on the use of interferometry. In this approach, a beam of light is directed onto the growing surface and the reflectivity of the sample is monitored as a function of time. Fig 19 shows the experimental arrangement of the system used to effect laser reflectometry (LR) monitoring of the growth rate. If the index of refraction of the growing layer is different than that of the substrate, the reflectivity will exhibit maxima and minima whenever the optical thickness of the growing film changes by one quarter wavelength. The period of a complete reflection oscillation is given by

$$T = \frac{\lambda}{2n_{eff}G} \tag{12}$$

where G is the growth rate and n_{eff} is the effective index of refraction of the growing material while taking into account the non zero incident angle. We have studied the use of various laser wavelengths as the probes for such a monitoring technique. The wavelength must be chosen so that it is not absorbed too strongly in any layer. This allows one to observe a few oscillations of the reflectivity before the extinction of the light is too great. Some absorption is desired however, so that the reflectivity signal represents a probe of just the top two layers, and is not a superposition of responses from many layers below the surface. Because of strong absorption in GaAs at shorter wavelengths (514 nm) and too little absorption at longer wavelengths (1.06 µm), the HeNe 633 nm wavelength was chosen as the optimum source. Initial experiments indicate that sufficient sensitivity in the reflectivity variation can be achieved to use this as a sensitive monitor of the growth rate of GaAs and AlAs and, as a consequence, $Al_{0.2}Ga_{0.8}As$. Initial results of this in-situ monitoring are shown in Fig. 20, where we

show the reflectivity at 633nm as a function of time for the growth of an AlAs/GaAs/AlAs structure. Note the large oscillations and the excellent signal to noise achieved.

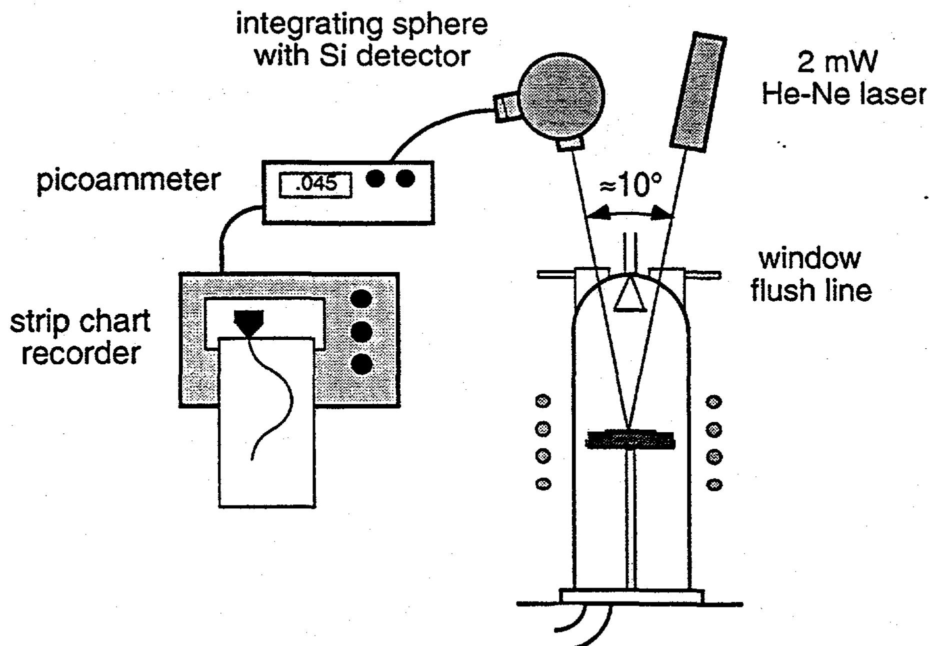

Fig. 24 Experimental arrangement used for in-situ laser reflectometry

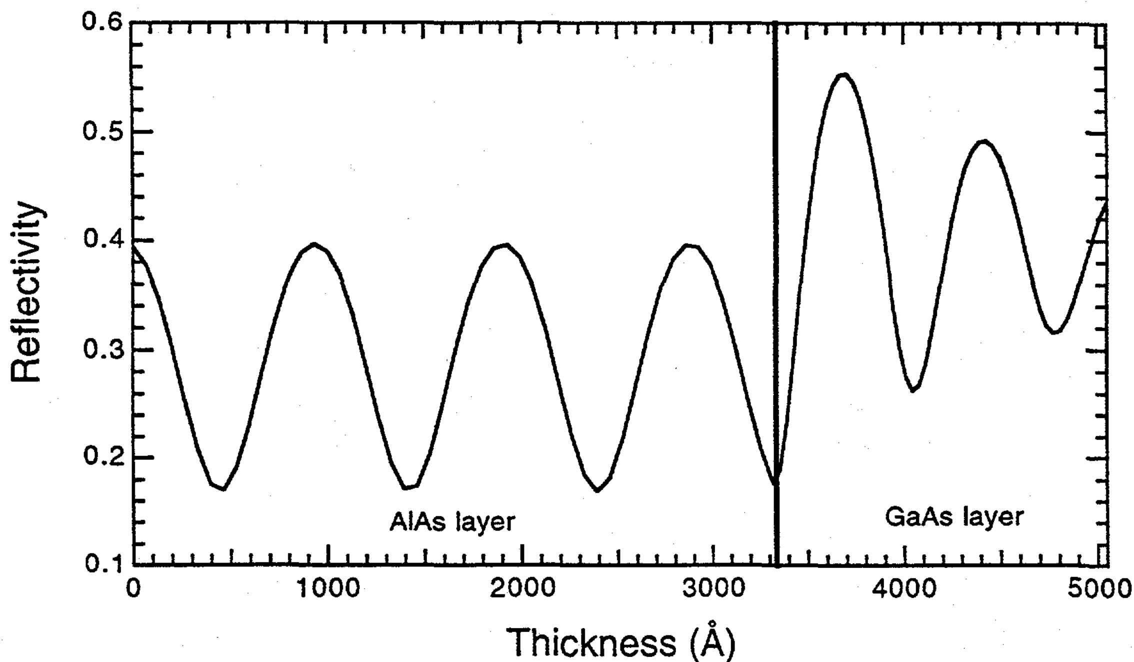

Fig. 25 Representative laser reflectometry data for AlAs and GaAs layers

Preliminary measurements showed an excellent correlation between the period of the oscillations and the growth rate. We set out to calibrate the index of refraction of

AlAs and GaAs at 633 nm and various growth temperatures by the growth of thick layers whose thickness can be measured independently and whose optical thickness can be observed by interferometry. These measurements led to the determination of the index of refraction at the growth temperature. The values for n_{eff} we use as working numbers at 750°C are 4.34 and 3.25 for GaAs and AlAs respectively. In the initial stages of use of this technique we calibrate the growth rate of one GaAs and and one AlAs layer at the approximate rates necessary to achieve a $Al_{0.2}Ga_{0.8}As$ composition. The growth rate of AlAs from the other Al source is then calibrated to allow us to grow the AlGaAs/AlAs reflector structures. Once the growth rates are known the time of growth of each layer can be adjusted to achieve the desired center wavelength of the Bragg reflector. During initial stages of this development, the determination of growth rates and subsequent adjustments were performed manually by the reactor operator. The subsequent implementation of a fully automated approach will be described below.

The approach described above was utilized to grow a series of binary Bragg reflectors to test the reproducibility of the growth rate. Table 2 below shows the comparison between the growth of binary Bragg reflectors with and without laser reflectometry (LR) monitoring.

TABLE 2- BRAGG REFLECTOR RESULTS WITH AND WITHOUT LR

Sample Number	Stop Band Center (nm)	Laser Reflectometry
1635	880	No
1637	980	No
1638	1040	No
1686	976	Yes
1692	976	Yes
1696	976	Yes

The reproducibility of the layer thicknesses are considerably improved through the use of LR monitoring. LR was also used to preset the composition of AlGaAs by determining the AlAs and GaAs growth rates associated with particular flow settings. These growth rates were adjusted to yield the desired composition by a linear extrapolation of the flow rates and these flows were used to grow the AlGaAs layer. Both the growth rate and the composition of the ternary layer agreed with the values predicted by the LR calibration of the binary compounds. $Al_{0.2}Ga_{0.8}As$/AlAs Bragg reflectors with a center wavelength at 0.84 μm were also grown with this approach that matched well the simulated spectra. In Fig. 26 a comparison between the calculated and measured laser reflectance spectra of a $Al_{0.2}Ga_{0.8}As$/AlAs 20 period Bragg reflector is

shown. The slight differences in the spectra as compared to the calculation result from nonuniformity in the grown layers. These layers were grown without rotating the sample during growth. Under these conditions our reactor yields materials with ±10% uniformity over a few centimeters. This observation presages our last difficulty with implementing the LR technique.

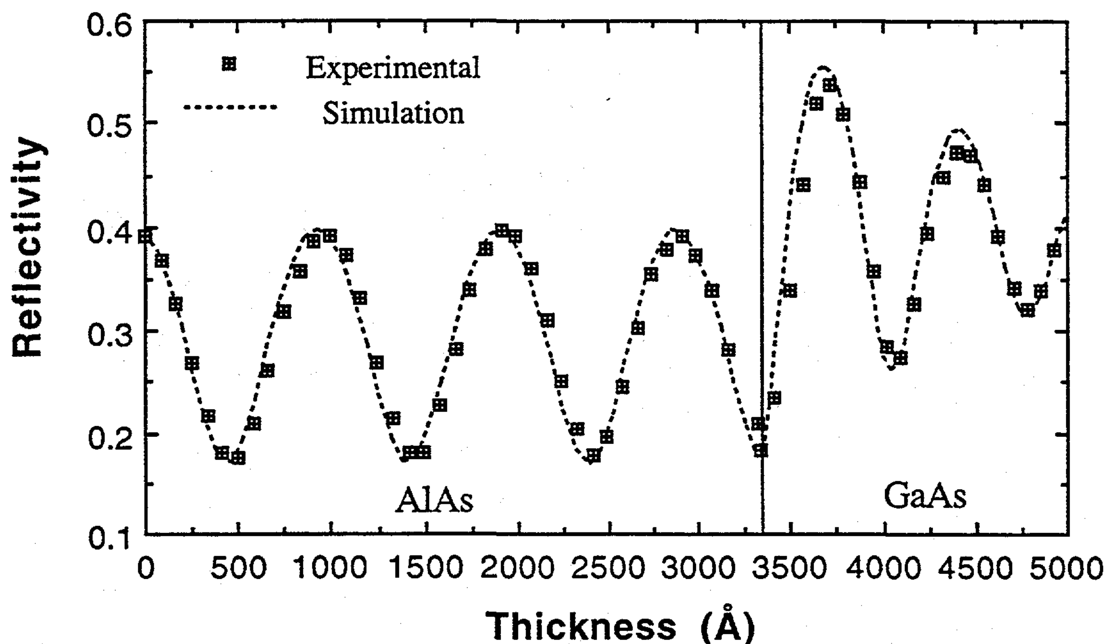

Fig. 26 A comparison between calculated and measured reflectance spectra

A problem with our current reactor set up is a precession of the susceptor and wafer that results from a slight misalignment of the rotation shaft on which the susceptor is mounted. This causes a precession of the reflected light about the output window and across the surface of the detector. To avoid this "noise" we have performed much of the LR characterization with a stationary substrate. This, however, results in nonuniformities that are too large for device use. The design of our reactor base and wafer mounting makes it difficult to perfectly align the plane of rotation of the susceptor without a major redesign of our reactor. We have installed an integrating sphere to collect the reflected light to reduce the signal variation that might result from a spatially nonuniform detector response but the major source of noise appears to come from nonuniformity in the glass windows. As the beam precesses on the output window, it encounters defects in the glass that, in turn, cause a variation of the signal. This "noise" is relatively high frequency compared to the LR signal upon which it is

superimposed. An example of LR data collected while rotating the substrate is shown below in Fig. 27. We have investigated using higher rotation speeds to increase the precession frequency, but the limit here is imposed by the tendency of the wafer to move on the susceptor at higher speeds. The presence of this run-to-run variable noise limits the precision to which LR can determine the growth rate.

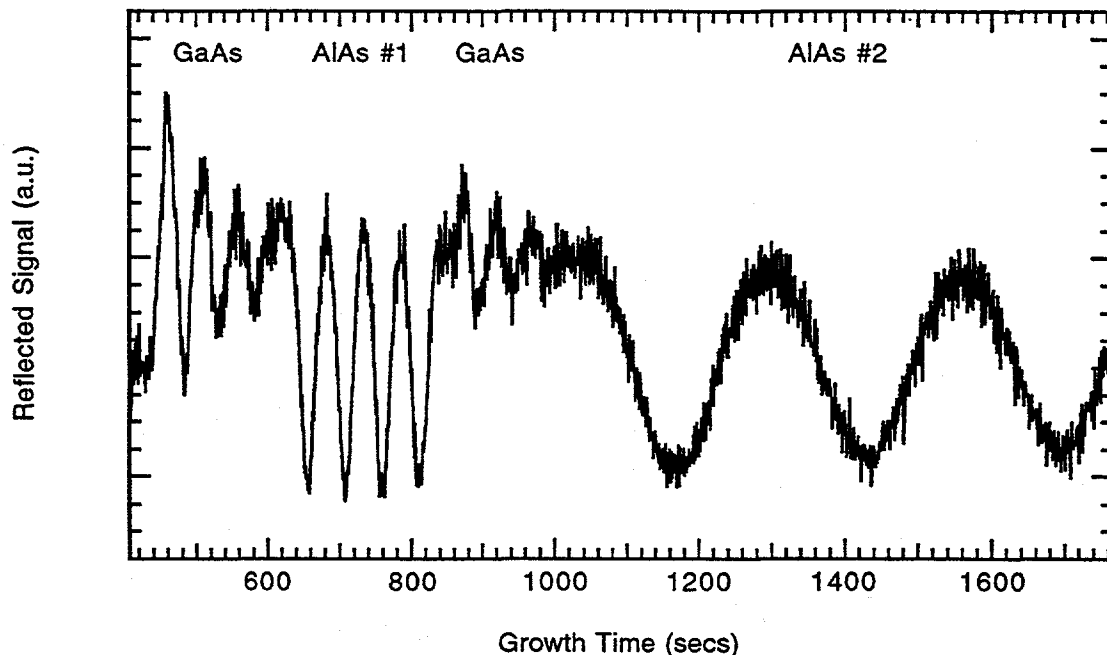

Fig. 27 Representative LR data collected during substrate rotation

In spite of the precession noise problem described above, we have succeeded in utilizing the LR technique to grow doped and undoped Bragg reflectors consisting of $Al_{0.2}Ga_{0.8}As/AlAs$ structures. Sufficient precision was achieved to again match closely the predicted spectra. The use of AlGaAs in the Bragg structure causes some compromises in the growth process. If we use only one Al source to grow both the AlAs and AlGaAs layers, the TMAl flow must either be kept constant during the growth of the reflector at the flow rate suitable for growing the AlGaAs portion of the reflector or it must be changed for each layer of the reflector. The former approach causes the growth time of the AlAs layers to be excessively long while the latter approach induces considerable inaccuracy in the growth of the various layers. We have changed the reactor design to incorporate two TMAL flows so that a separate flow can be arranged for each layer of the Bragg.

In order to integrate the LR technique into normal growth procedures as an automated tool, it is necessary to extract the reflected signal from the noise in a reproducible way. The first step was to install the appropriate hardware so that digitial

LR data could be recorded and analyzed by the reactor control program. The voltage output from the picoammeter used to read the detector was connected to an A/D port in the interface module used for reactor control. The reactor control program was then completely rewritten from the ground up in order to integrate the additional code required for LR implementation.

Some initial attempts to limit the noise through the use of simple RC filters were unsuccessful. Although the peak-to-peak magnitude of the noise was reduced, the remaining noise was still too large to utilize simple peak finding as a method of determining growth rates. The frequencies involved (<2 Hz) limits the applicability of phase-sensitive techniques. It was decided that nonlinear curve fitting techniques would be used to extract the LR signal. A stand-alone application was written and used to evaluate various curve fitting methods. The general approach of nonlinear fitting involves the minimization of a nondimensional merit function χ^2 by evaluation of best-fit parameters. The nonlinear nature forces the minimization procedure to occur iteratively. The procedure searches a three dimensional space and looks for points of minimization. The iterative improvements then allow the routine to find the lowest local point for a solution. The Levenberg-Marquardt method was chosen for this task, since it has demonstrated good performance in practice and has become the standard of nonlinear least-squares routines.[3]

A sinusoidally varying function and its derivatives are required to fit the LR data. The relation is as follows:

$$y = K0 + K1 * \sin(K2 * x + K3) \tag{13}$$

where x is elapsed run time and y is the voltage value returned from the picoammeter. K2 is the most important value for our purposes, since it is used to determine the growth rate. Due to the nonlinear nature of the Levenberg-Marquardt algorithm, providing accurate first guesses to initialize the fitted variables K0-3 are imperative to the success of the fit. Noise-free data is needed to make these estimations, so the data is first smoothed using a multipoint window passed 24 times over the raw data. Then the crossing points are determined relative to the start time of the particular layer being evaluated. The crossing points are defined as the x (time) values in each sinusoidal curve where the data crosses the median value of the time range being processed. The position (K2) and phase (K3) variables are determined from these values. The amplitude variable (K1) is simply half the difference between the maximum and minimum in the smoothed data. K0 is initialized as the RMS average value of the smoothed data, and is held at that value during the fitting procedure.

The fitting algorithm was optimized and integrated into the reactor control software. The interface allows the operator to choose how the growth rates determined during the calibration layers are utilized in the modification of subsequent layers. Either time or flow modifications are allowed. A graphical description of the automated LR algorithm is shown in Fig. 28. Some example results of automated LR data fitting is shown in Fig. 29.

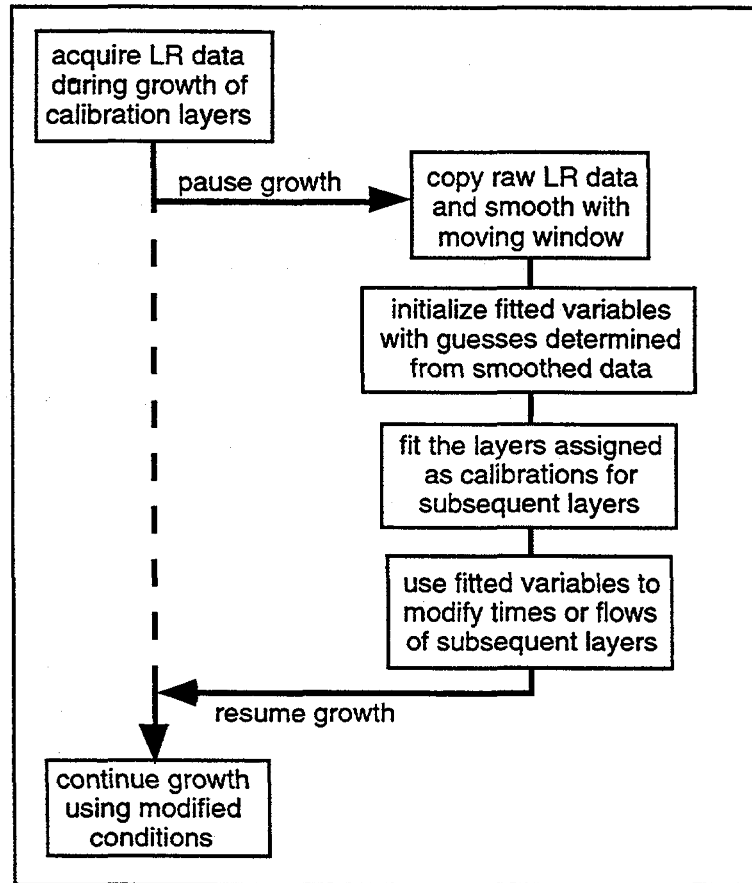

Fig. 28 The automated LR algorithm as implemented in USC's reactor control program

The automated LR technique has proven to be very effective in the reproducible positioning of DBR stop bands. The mathmatical algorithm is robust and exhibits a very high success rate in determining the proper growth rate. Extremely noisy data can still be problematic, and may result in incorrect growth rate determinations. The reason this happens is that the initial guesses are incorrect, due to noise spikes being interpreted as median cross points. The merit function is still minimized, but at a point away from the local minimum with physical meaning.

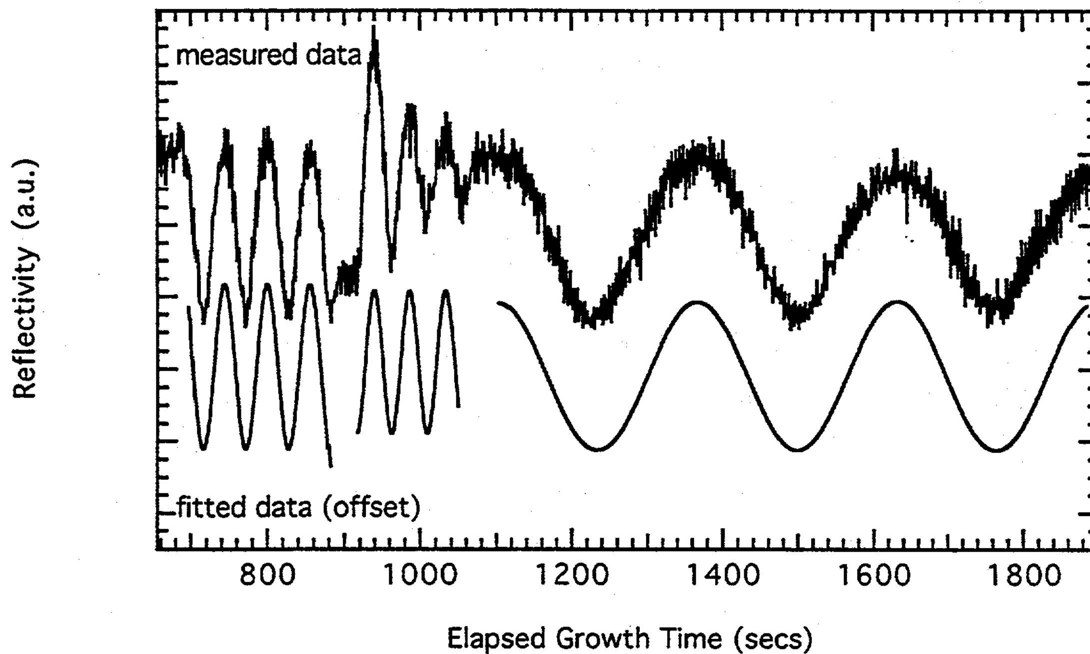

Fig. 29 An example of GaAs and AlAs layers and the nonlinear fits to the data.

There was some concern that the accuracy of automated LR would be compromised when high doping was used, since the index values we determined for GaAs and AlAs at 750°C were measured with intrinsic samples. To minimize the resistivity of DBRs located within device structures, however, doping levels above 10^{18} cm^{-3} are required. The effect of high doping levels proved to be minimal. As shown in Fig. 30, automated LR works very well at positioning both binary (0.98 µm) and ternary (0.84 µm) DBRs which are highly doped.

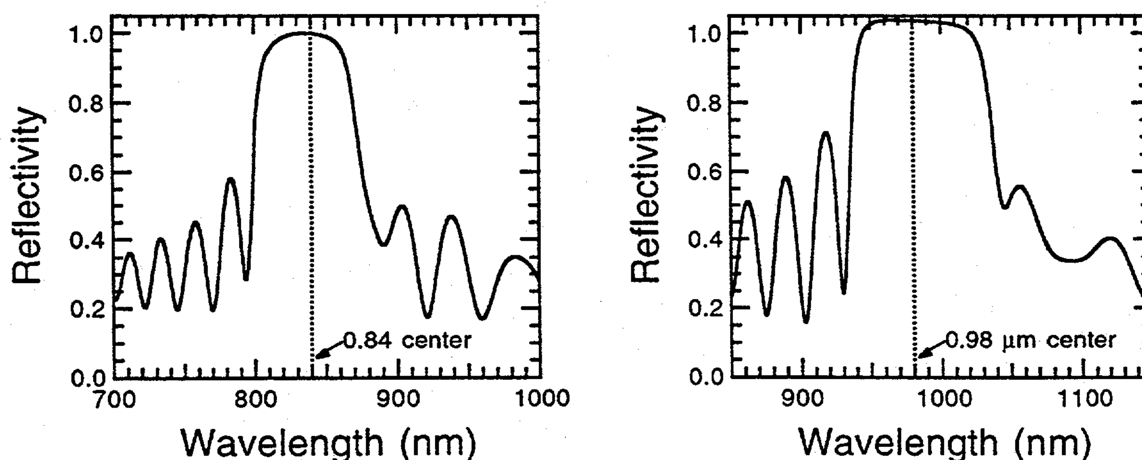

Fig. 30 Examples of highly doped binary and ternary DBR structures grown using automated LR.

Task 3: Solar Cell Fabrication and Characterization

At the start of this project, an arrangement with Varian had been made to provide fabrication and characterization support. Unfortunately, Varian left the solar cell business and USC was forced to develop its own expertise.

A high efficiency solar cell requires metallized contacts of low resistivity to maximize the power delivered from the device. There are two different metallizations schemes necessary for our device; a p-type contact patterned on the top of the device as a bus bar and fingers, and an unpatterned n-type contact on the bottom covering the substrate surface. The p-type contact is composed of sequential layers of Cr and Au. The primary role of the Cr layer is to improve adhesion of the overall metallization, and a thickness of 100Å has proven adequate. The Au layer deposited on top of the Cr is used for probing, and therefore should be as thick as possible without interfering with the lift-off procedure used to define the finger regions. The n-type bottom contact is deposited over the entire substrate surface and experiences no patterning. A AuGe/Ni/Au sequence is utilized, with the thicknesses of the AuGe, Ni, and Au layers being 1600Å, 400Å and 2500 Å respectively.

An alloying step is required to promote the diffusion of Ge atoms into the GaAs substrate. However, this heating step can be detrimental to the ohmicity of the Cr/Au contact. This is due to the reaction of Cr atoms with any residual oxides or oxygen atoms present at the semiconductor-metal interface or within the Cr layer itself. The Cr-O complex that forms at the surface during the heating step acts as an energy barrier to any carriers passing through the region, and increased resistivity results. The alloying step required for the n contact therefore needs to be performed prior to the p contact deposition.

We experimented with various alloying schemes to determine optimal conditions for providing the low resistivity. Resistivity was determined using the transmission line method (TLM), which consists of a top-side metallization pattern consisting of six square probe pads of equal area which are separated by varying distances. TLM samples were prepared both with and without oxide-removing pre-etches (dilute $HCl:H_20$ solution) performed just prior to evaporation. Small improvements were generally observed on etched samples. The metals were deposited by electron beam evaporation at a chamber pressure less than 3×10^{-7} torr. Alloying temperatures were varied from 350°C to 450°C. Temperatures below 390°C proved ineffective in providing ohmic behavior in the n-type contacts. An alloying temperature of 420°C was chosen for all subsequent alloying tests to insure that the eutectic temperature of approximately 390°C required to activate a AuGe type contact would be exceeded while exposing the

sample to minimal total heat exposure. The resistance between each pair of pads was then measured and plotted as resistance vs. separation distance as shown below in Fig. 31.

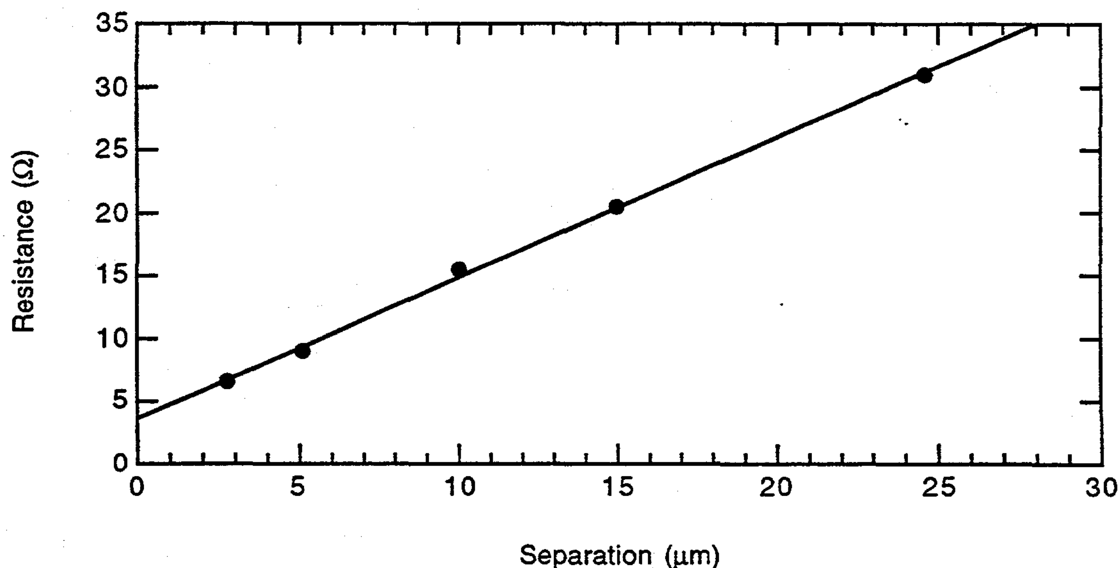

Fig. 31 A plot of resistance vs. distance between contact pads

The slope and intercept of a line fitted to the data is then used to determine a contact resistivity for the sample following the approach of Berger[4] as:

$$r_c = \frac{(R_c)^2 z}{slope} \tag{14}$$

where R_c is the contact resistance extrapolated at 0 separation distance and z is the width of the contact pads. The units of r_c are Ω-cm^2. The data measured for the n- and p-type meatallizations described above is shown in Fig. 32. Note that the p-type Cr/Au contact is damaged almost immediately by the application of temperature. The resistivity of the n-type AuGe/Ni/Au contact drops almost three orders of magnitude after as little as 10 secs of heat. The minimum resistivity values achieved are 1.1×10^{-6} Ω-cm^2 for the AuGe/Ni/Au contacts, and 3.0×10^{-6} Ω-cm^2 for the Cr/Au contacts. These values are quite good, and certainly sufficient for use in high efficiency solar cell devices.

Although our laboratory has experience with the wet etching requirements of semiconductor lasers and transistor devices, there was no previous experience with etching recipies used for solar cell applications. There are two etching procedures required in the processing steps of a solar cell; the selective removal of the GaAs cap layer and isolation of the individual devices. Most of the devices fabricated in this

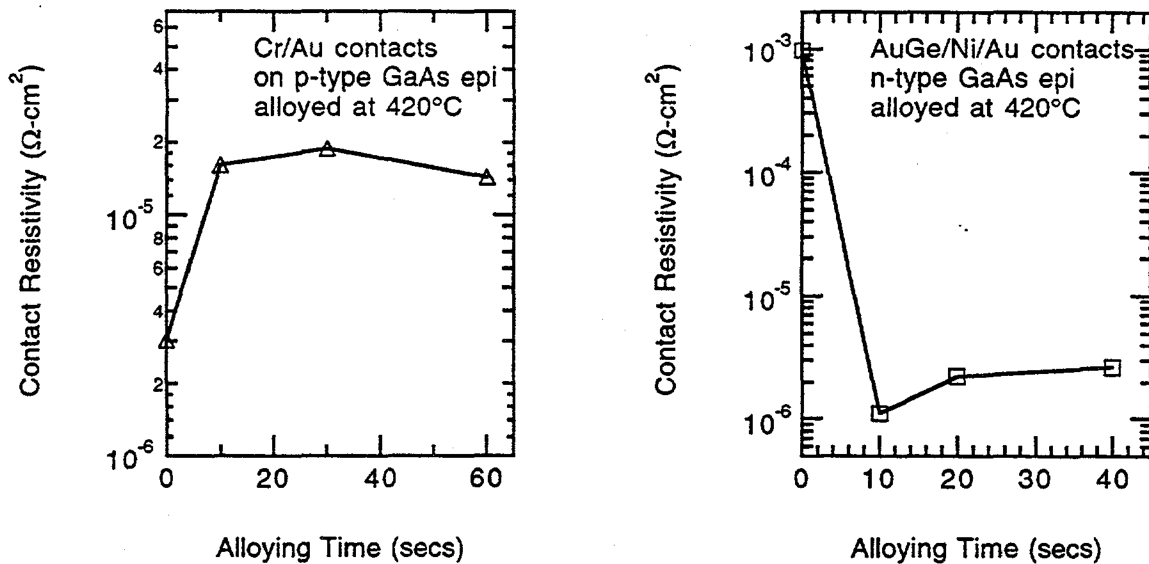

Fig. 32 Contact resistivities for p- and n-type metallizations at different alloying times

project are 5 mm on a side, providing an area of 0.25 cm^2. Some smaller devices (0.1 and 0.01 cm^2) devices were also processed. The distance between each device is approximately 2 mm, which is relatively large and provides for easier etching. A good etch should remove various compositions of AlGaAs materials at essentially equal rates, thereby providing a smooth side wall. It should also etch without generating a large undercut. The viscosity should be minimized so that the etching process is not limited by the diffusion of fresh etchant to the etch site.

We investigated four different etchants used for mesa isolation. The first is 8:1:32 (H_2SO_4:H_2O_2:H_2O). The proportion of acid is much greater than oxidant, so this etch is probably controlled by the rate of oxidation. This is a disadvantage, since high aluminum composition materials oxidize more readily, and therefore will be etched more quickly and uniformly than low aluminum materials. This was demonstrated in practice. Several different samples were used, including an N+ GaAs substrate, a 25 pair DBR of $Al_{0.2}Ga_{0.8}As$/AlAs, and a structure consisting of two layers (each 1.5 μm thick) of $Al_{0.8}Ga_{0.2}As$ and $Al_{0.5}Ga_{0.5}As$. The 8:1:32 etching solution was cooled to room temperature after mixing, and the solution slowly stirred. The solar cell mesa isolation mask was used to define the trenches to be etched. Dektak profiles of the etched channels were measured after the etching procedures. The GaAs substrate sample appeared very anisotropic, with deep troughs at the edges of the etched channels. In addition, the channel shapes were very dependent on the orientation of the channel to the stirring direction. The approximate etch rate was 175 Å/s, where the overall depths

were taken from the center of the channel. The DBR sample also etched anisotropically, but the overall etch was smoother than the GaAs samples. The bottoms of the etched channels were still rough, indicating some nonuniform etching. The overall etch rate was approximately 190 Å/s. The best etch results were obtained on the high aluminum sample, where the etch surfaces were smooth, and the etch appeared isotropic and relatively insensitive to stirring direction. It is apparent from these data is that the 8:1:32 etch is inappropriate for solar cell isolation due to its diffusion limited, nonuniform etching behavior on low aluminum composition materials.

Another sulfuric acid based etch with the proportions 3:1:1 (H_2SO_4:H_2O_2:H_2O) was briefly used. The amount of acid and oxidant are roughly equal in this case, with a little water added to cut the viscosity of sulfuric acid. Etchants with equal values of acid and oxidant tend to be quite aggresive, and this is the result seen in our samples. Samples etched included DBRs and several complete solar cell structures. All etched channel bottoms were very rough, with deep troughs near the device walls. Not surprisingly, this etch was also sensitive to stirring direction. This etch is also inappropriate for device isolation.

Good results were achieved with two additional etching solutions. A four component etch mixed in proportions 3:1:1:1 (MeOH:H_2O:H_2O_2:H_3PO_4) has been reported in several publications concerning solar cells.[5] The solution is made quite thin by the methanol, which generally allows for uniform etching without stirring. This mixture provides relatively smooth surfaces, although there are some shallow troughs near the device edges, and the bottom of the channels are slightly bowed. The overall etch rate was measured to be 145 Å/s. An etch used by Giles[6] to isolate vertical cavity laser devices was also tested. It is mixed with proportions 1:5:15 (H_2SO_4:H_2O_2:H_2O), which should provide isotropic etching due to the high ratio of oxidant to acid. The high water content makes it less viscous, which helps supress diffusion limited anisotropy and provide smooth edges without stirring. The etched channels appeared smoother and more uniformly etched than all the other etchants used. The etch rate is quite fast (425 Å/s) but it is reproducible. This etch was used in all subsequently processed solar cell samples for device isolation.

For the selective removal of the p+ GaAs cap layer, an etch is required which has very high selectivity for GaAs materials over Al-containing alloys. The p+ layer is used on top of the 80% AlGaAs window layer to promote good contacting to the metallized fingers. The processing procedure is simplified if the metallized fingers are used as the etch mask, and that is the procedure used here. We investigated the use of both citric-acid and ammonium hydroxide based selective etches. The citric acid solution is

prepared by first mixing powderous $C_6H_8O_7$ with H_2O (1g to 1 ml), and then diluting 4 parts this mixture with 1 part H_2O_2. Selectivities of 1000 have been reported for this etchant on AlAs, but it is slightly lower for 80% AlGaAs[7]. We used this etch with good success after overcoming several initial problems. Although cleanly etched surfaces were generally observed, small unetched portions near the finger edges occasionally remained. In addition, the etching times varied from sample to sample. We observed that periodic rinsing of the samples during the etching procedure helped keep etch times more uniform, and the edges more cleanly defined. What provides the best result is to dip the sample in warm, dilute (1:20) HCl prior to placing the sample in the citric solution. At intervals of 30 seconds or so, remove the etching sample from the citric solution and place it in the HCl solution for several seconds, then resume the citric etch. This added step completely removes the gummy residue generated by the cirtic etching process, and leaves a clean surface for continued etching. Once these initial problems were overcome, the cap removal left clean sidewalls with minimal undercut, and smooth surfaces between the finger mesas. An additional selective etch that was tested is a 1:19 mixture of $NH_4OH:H_2O_2$. Sahara[8] has used this successfully as a GaAs specific etch, although no measured selectivities are available. The results obtained with this solution are unacceptable, due to undercutting of the finger regions. This may be due to the extremely fast etch rate of 800 Å/s. This citric based etchant was used for cap removal in all subsequent device processing.

A high performance AR coating is imperative to efficient solar cell devices. A two layer coating composed of ZnS and MgF_2 has become a standard for high performance cells, and we have utilized this coating as well. We have the ability at USC to deposit these materials by thermal evaporation, which has been shown to be superior to electron beam evaporation for devices sensitive to the damage potentially caused by high energy procedures.[9] In order to design the optimal coating, the reflectivity was modelled while considering the both the index and absorption dispersion of the $Al_{0.8}Ga_{0.2}As$ window layer and GaAs layers underneath. Since the window layer is only 300Å thick, it is critical to include it in any coating simulations. An optimized coating is shown below in Fig. 33.

The solar cell device characterization performed for this project consists of three components: dark IV, light IV and spectral response. All testing capability is assembled into one multi-component system, and a software program has been developed to provide test procedure automation, data analysis, and output of all results in both tabular and graphical form. All devices were mounted on thin Au-coated ceramic sheets with high electrical and thermal conduction. A small vacuum chuck is used to

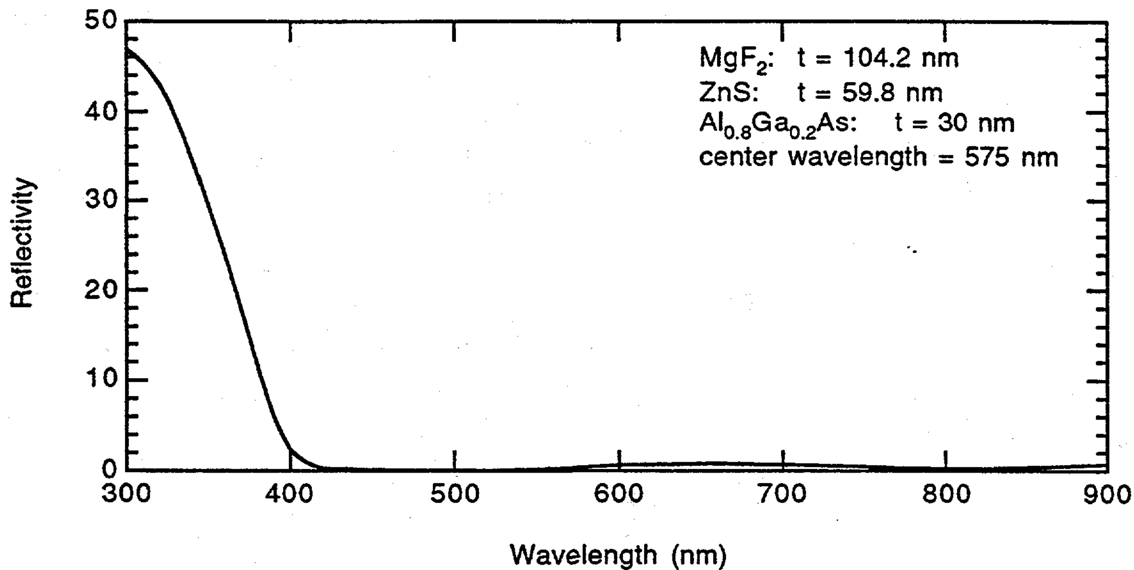

Fig. 33 An optimized 2 layer AR coating composed of ZnS and MgF_2

mechanically mount the device under test (DUT) in the probing position. Electrical connection to the cell cathode is provided by a wire soldered to the surface of the ceramic plate material and connected via a BNC connector. Two probes are available to contact the anode of the DUT. One probe delivers a voltage bias, and the other probe is used to measure the current of the cell. The current is determined by measuring the voltage present across a precision 0.75 Ω resistor, which keeps the load on the device at a minimum. With a current of 7 mA flowing, there is only 5 mV of drop across the resistor. One-sun illumination is provided by a 100 W ELH lamp positioned approximately 6 to 12 inches from the probe station surface. It is driven at 115 Volts by a regulated high power DC supply. The optical power density is set to 100 mW/cm^2 by modifying the distance of the lamp from the cell with a translation stage such that the Jsc of a calibrated solar cell matches the value provided by NREL.

The spectral repsonse is measured using a chopped source of monochromatic light and a lock-in amplifier. The device is light biased with the ELH lamp (at 0.5 mA device current) while under short-circuit conditions. To provide a range of wavelengths, a Xe arc lamp is focussed into a 1/8 meter monochrometer outfitted with a 1200 line/mm grating blazed at 400 nm. The output slits are set to provide 4 nm of output bandwidth. The "monochromatic" light is delivered to the surface of the DUT using a large core silica fiber. The 700 μm core diameter provides good coupling when combined with a microscope objective at the output of the monochrometer. The other end of the fiber is positioned slightly above the sample at a distance of approximately 3 mm. Since the cleaved fiber end delivers light at a high angle of divergence, close positioning will

deliver the most optical power to the device. Both ends of the fiber are mounted on precision verniers for accurate and stable alignment. The ELH lamp is not positioned normal the the device surface (as in light IV tests), but at a slight angle to minimize shadowing of the fiber arrangement. The chopper is operated at 350 Hz, and the current output of the DUT is fed into a high dynamic range lock-in amplifier for measurement.

The optical power at the tip of the fiber is evaluated using an NBS-traceable calibrated detector with a range of 250 nm to 1150 nm. Since calibrations are provided every 10 nm, these wavelength positions are used during the spectral response measurement. The Xe lamp output must be steady during the measurement cycle, so it is driven with a very stable power supply. The positioning of the fiber input at the waist of the beam exiting the microscope objective is also very critical. A precision x-y-z translater was installed after the drift of a less precise unit proved responsible for reproducibility problems. The output of the entire optical train (lamp, monochrometer, fiber) is measured across the range of wavelengths from 300 nm to 1000 nm before every device scan. The distance of the fiber tip to the detector surface is set to the same value as the tip to cell distance. Once the light source is calibrated, the fiber end is positioned over the solar cell, and the white light source set so that 0.5 mA of current is being delivered by the device. The monochrometer is then scanned through a range of 300 nm to 1000 nm, and the current induced by the modulated light source is compared with the optical power being delivered to the surface of the device. Because the wavelength range being used is large, second order wavelengths appear as part of the light output when the monochrometer is set at wavelengths greater than 600 nm. An RG610 optical filter is placed in the optical path at this point, which blocks out nearly 100% of light with wavelengths less than 610 nm.

The choice of a Xe arc lamp instead of a tungsten-halogen lamp for spectral response measurements was made primarily because of the greatly increased optical power delivered through the monochromator. The Xe lamp can be focussed tightly at the input slits of the monochrometer, while the TH lamp cannot. The increased optical modulation of the cell being tested greatly enhances the lock-in amplifiers ability to extract a proper current value. In addition, the Xe lamp has much more output at wavelengths less than 500 nm. The disadvantage of this arrangement is that arc lamps have very spiky output in the near IR. With small misalignments in grating position between the lamp calibration and device measurement scans, the resulting SR data can appear spiky in the near IR region. All QE data shown is normalized to the maximum point taken during the particular scan, since making absolute measurements with the arrangement described above is quite difficult.

The solar cells fabricated in the earlier stages of this project exhibited poor performance. The morphology of the epitaxial materials being grown at the time was poor, with defect densities often greater than 2000 cm^{-3}. The surface micrograph of an EOR structure (sample 2228) shown in Fig. 34 represents a worst case sample. The magnification is 100 X, and the defect density in this case is about 25,000 cm^2. Light IV results from devices fabricated on these materials display low V_{oc} values and poor diode characteristics as shown in Fig. 35. In addition, dark IV measurements exhibit large shunt currents. Various efforts to modify wafer preparation, epitaxial growth and processing procedures did not reduce the defect density significantly. It was observed across several batches of processed cells that device performance parameters appeared to scale with defect density. An SEM micrograph taken at 6 KX of a representative surface defect is shown in Fig. 36. The defect appears granular in shape, and is approximately 3-5 μm in width.

Further investigation into the cause of these defects was initiated in hopes of revealing their cause. Through EDAX and Auger analysis combined with localized Ar^+ milling capability, it was determined that the defects were composed mainly of zinc and aluminum oxides. The presence of oxides in MOCVD material suggests a leak or source purity problem, which allows water or oxygen to enter the system. As compared to horizontally configured or low pressure reactors, the hydrodynamics associated with

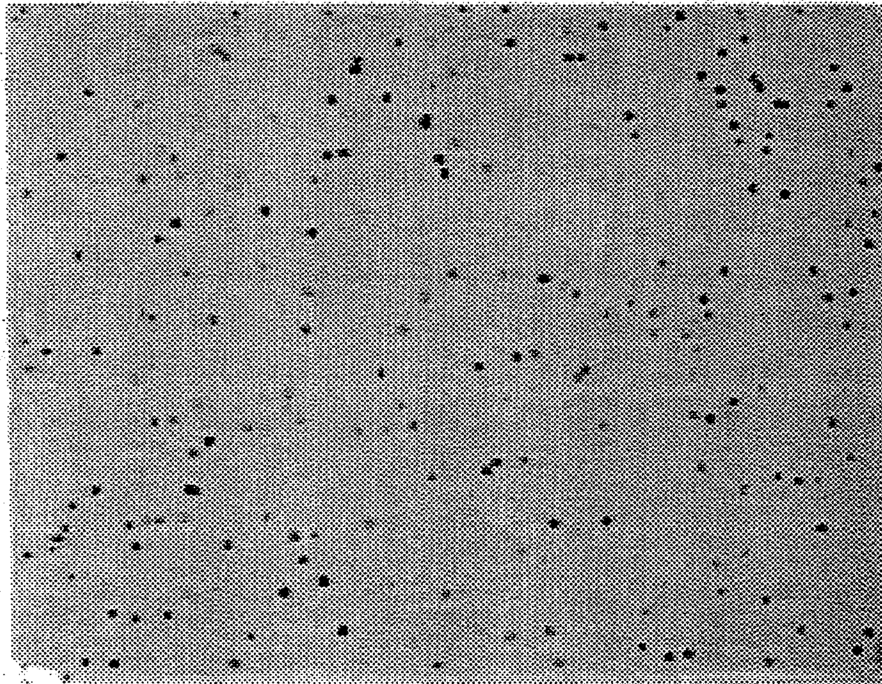

Fig. 34 An example of surface morphology dominated by particle-induced surface defects. Magnification here is 100X, with the defect density approximately 25,000/cm^2.

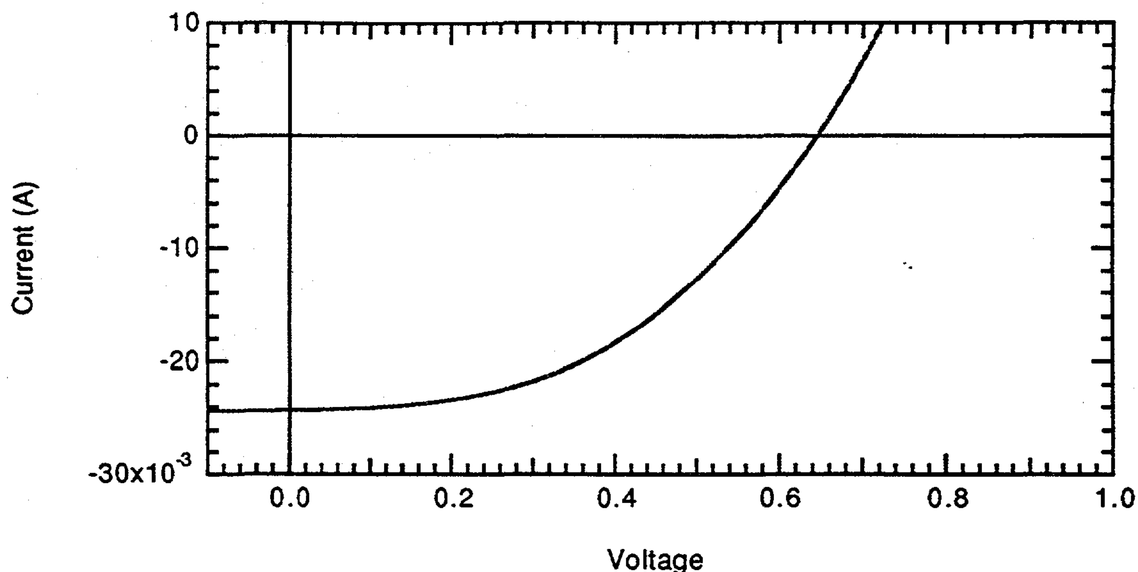

Fig. 35 A representative light IV of early cells. Note the low V_{oc} (1 V expected) and poor fill factor. A calibrated light source was not used in this measurement. Illumination intensity equals approximately 4 suns.

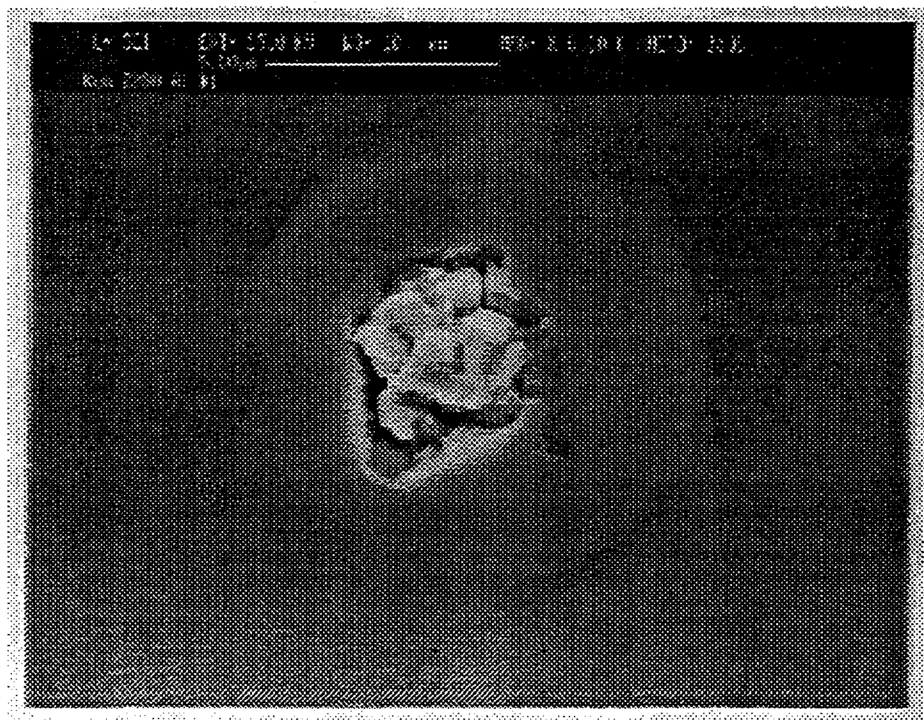

Fig. 36 SEM micrograph of a representative surface defect of approximately 3-5 μm in width. Notice the granular structure.

the vertical configuration of our MOCVD reactor tends to enhance the generation of particles and minimize the incorporation of oxygen as a contaminant in the growing crystal lattice. This is due to a combination of increased turbulence at the reactor inlet

caused by the quartz baffle, and hydrodynamic eddy currents enhanced by radiant heating, both of which increase the residence time for gaseous source materials. This promotes the reaction of the pyrophoric metalorganic source materials and the oxygen/water contaminants, creating oxide particles in the process. The effect, therefore, is that the overall quality of the semiconductor materials is high due to the passivating effect of the particle generating reactions, but the diode performance is degraded by shunt currents caused by the particle defects themselves.

Leak checking of the entire gas handling system was performed, which revealing that the hydrogen purifier cartidge had failed. This allowed "wet" hydrogen to pass unpurified, allowing the metalorganic vapors produced during source transfer to cause a build-up of powderous deposits throughout the system downstream from the source bubblers. The gas handling system was dismantled, cleaned and rebuilt, and another hydrogen purifier cartridge was installed. In addition, the DI water system in the growth lab was flushed and sanitized to reduce the possibility of defect generation due to surface particles reamaining after substrate rinsing.

The morphology of the epitaxial materials grown after these extensive efforts was vastly improved, with defect densities of less than 100 cm^2 often achieved. Devices processed from these materials were AR coated and mounted for testing. Dark IV results were encouraging, but not optimal (see Fig. 37). Saturation current densities were extrapolated from dark current (A/cm^2) vs. bias voltage data by fitting the appropriate range of data while allowing both the intercept and slope to vary. The ideality factors n_1 and n_2 were not held at the theoretical values of 1 and 2 in these fits. The values determined for J_{01} using this approach were 4.61×10^{-15} (HBF) and 1.58×10^{-15} (EOR) with associated ideality factors n_1 of 1.34 and 1.28 respectively. These values of J_{01} are slightly higher than desired, since values have been measured as low as 2.3×10^{-20} on MOCVD material. Since we are fitting dark J-V data, series resistance may play a role in determining the slope, thereby raising the J_o values slightly. However, it has been shown that in devices with low series resistance, the dark J-V and log J_{sc}-V_{oc} curves are identical at low current densities. Therefore, our data should be adequate in determining accurate saturation current densities. These numbers suggest excessive recombination in the bulk material, which we believe is due to the presence of the granular defects. The fitted values for J_{02} were quite good at 4.17×10^{-12} (HBF) and 1.33×10^{-12} (EOR) with ideality factors of 1.8 and 1.69 respectively. These values are equivalent or better than the best published values for similar devices. This suggests good quality p-n junctions and peripheral surfaces with low effective recombination velocities. Although the n=1 currents remain high, they are three orders of magnitude

lower than previously tested cells with much higher defect densities. We believe the reason for the decrease in J_{01} is the continually improving state of the epitaxial material and a steady decrease in defect density. The trend of slowly improving material quality after major reactor maintenance has been observed before in MOCVD. However, there is room for improvement.

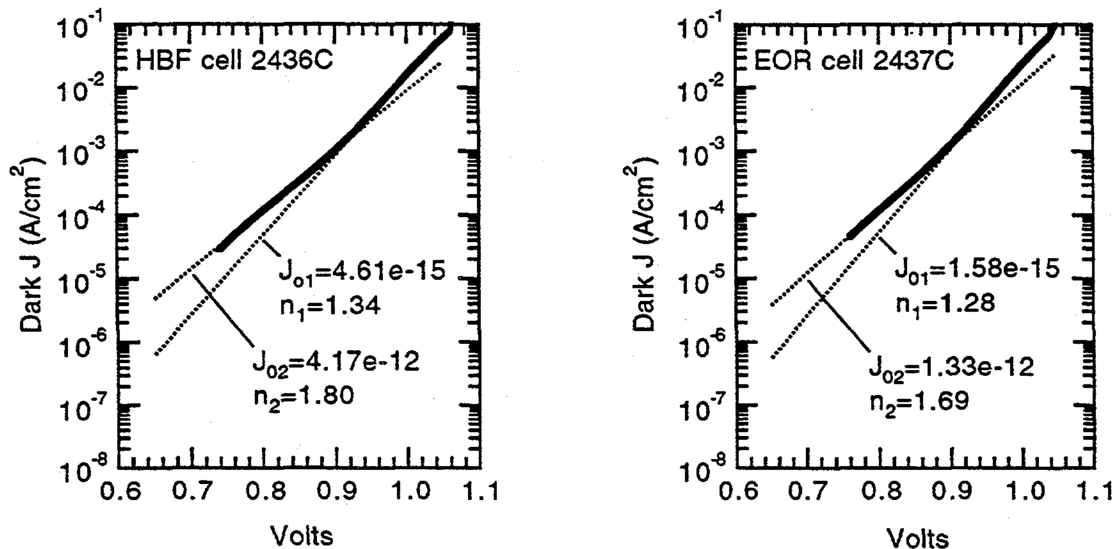

Fig. 37 Dark log J-Vs of the best HBF and EOR cells to date

Solar efficiency (η_S) was determined from illuminated IV data, which was measured using an ELH lamp source whose total optical power density was calibrated by matching the I_{SC} value of a calibrated GaAs cell provided by NREL. Curves from the most efficient HBF and EOR cells tested to date are shown in Fig. 38, and a summary of performance parameters is listed in table 3 below. The V_{OC} values are 30-40 mV lower than predicted from simulations on similar structures, which we believe is attributable to the excessively large dark currents measured on all cells. Despite slightly low V_{OC} and J_{SC} values, the overall efficiencies of these devices are good, with η_S values of 21.51% (HBF) and 20.01% (EOR). These results are not spectrally corrected, however, and have not been confirmed at this time using an illumination source more representative of AM1.5G. The fill factors are very good, equalling or exceeding the best values published and approaching the theoretical maximum of 0.88. This implies devices with low series resistance, and also indicates that the solar efficiency of our cells is not limited by factors relating to the squareness of the I-V curves. We believe the efficiencies to be limited by the effects of high dark currents and low J_{SC} values.

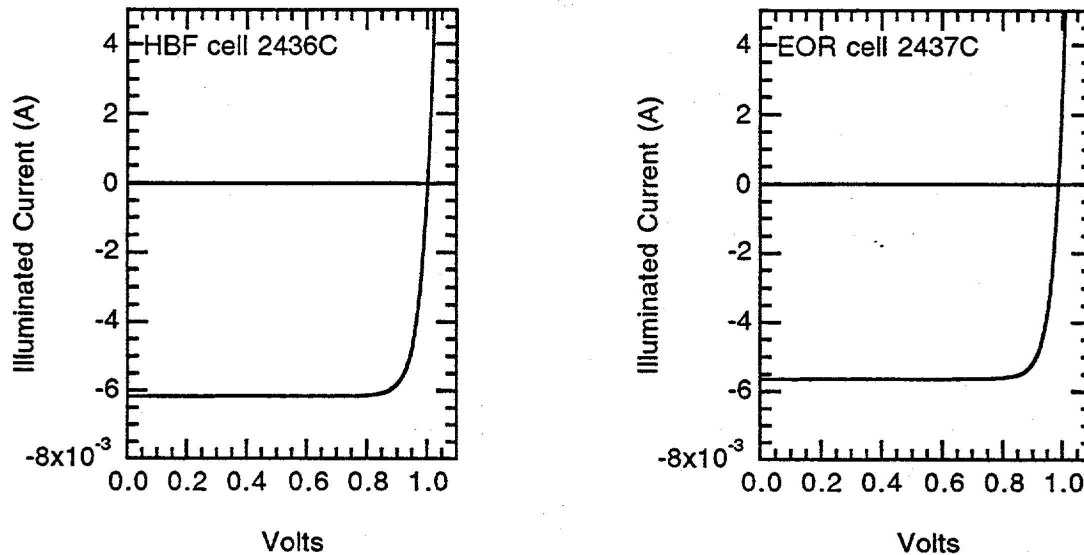

Fig. 38 Light IVs of the best HBF and EOR cells to date (taken under 100 mW/cm^2)

Parameter	HBF cell	EOR cell
V_{oc}	1.002	0.985
J_{sc} (mA/cm^2)	25.33	23.69
Fill Factor	.848	.857
Efficiency	21.51%	20.01%
J_{o1} (A/cm^2)	4.61×10^{-15}	1.58×10^{-15}
J_{o2} (A/cm^2)	4.17×10^{-12}	1.33×10^{-12}

Table 3 Performance parameters from the best HBF and EOR cells tested to date. All results measured with 100 mW/cm^2 ELH lamp.

Spectral response measurements indicate the efficient collection of photons across a full range of energies, but possible measurement artifacts limit our ability to quantify the advantages of the EOR design. As discussed previously, a Xenon lamp source was chosen due to the total optical power available and the increased measurement sensitivity provided. The Xe emission spectra contains large spikes, and these are plotted along with some normalized quantum efficiency data of representative HBF and EOR cells in Fig. 39. Each QE data set is normalized to the largest point measured in that particuar scan. Note the large optical power peak at 830 nm. This peak corresponds exactly with the small rise in QE observed over a large number of measured HBF and EOR devices. Since we are measuring relative, not absolute quantum efficiency, this bump will certainly affect the position of all other points on the QE axis, making comparisons of responsivity between different devices difficult. The cause of this spike was initially thought to be slight wavelength misalignments between the separate

power calibration and device measurement scans used in our measurement approach, but the frequency and reproducibility of the peak characteristics seem to rule out that possibility. The DUT is light biased using the ELH lamp in order to saturate any traps or other recombination sites that may affect an unbiased SR measurement, which would lead to results not indicative of performance under actual operating conditions. The amount of light bias chosen for our initial SR measurements was 0.5 mA delivered device current, since this is how the calibrated cell received from NREL was measured. This is a fraction of the normal 6-7 mA current produced under 1-sun illumination, and although it represents much more power than the chopped, single wavelength optical excitation, it was thought that it may not provide adequate quenching. The large change in optical power absorbed by the device during the wavelength change from 810 nm to 830 nm may serve to saturate previously unsaturated recombination centers, thereby providing an slight increase in efficiency. It was hoped that additional light bias might smooth the results. This hypothesis was tested by remeasuring several previously tested devices while under a light bias of 5 mA. The data shown below were measured with a light bias of 5 mA device current, but the peak at 830 nm remains in the HBF sample. The EOR device exhibits a peak at 850 nm and a dip at 830 nm. It is therefore difficult to positively quantify the effect of the DBR on the bandedge response of the EOR cell using the present data. It appears that the band edge response of the EOR cell is increased, but the peaks on both curves are suspicious and perhaps not representative of the physical device response.

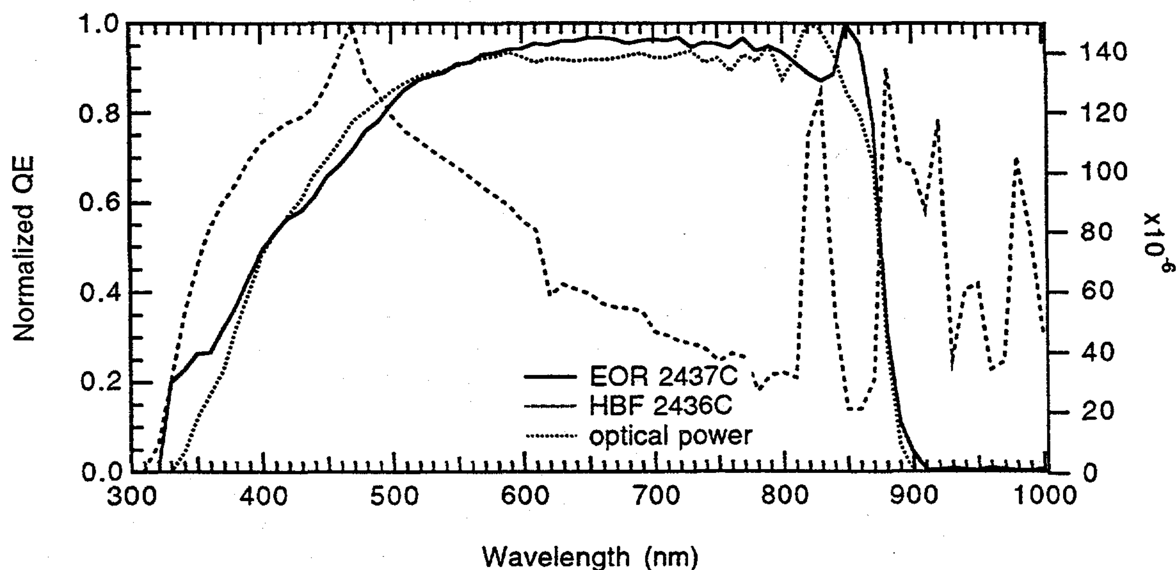

Fig. 39 Normalized quantum efficiencies of representative HBF and EOR devices measured under 5 mA light bias. plotted along with the optical output of the Xenon lamp used in the measurement

It appears that our SR measurements should be confirmed using a light source with smooth output in the near IR. A 100W TH bulb compatible with our monochromator system has been obtained, and will be tested in the near future. The raw (unnormalized) data (Fig. 40) is very similar to the normalized data. The important point here is that the response of the two cell structures is almost identical, even though the EOR cell has a base half as thick (1.5 μm) as the HBF cell. This provides strong qualitative evidence that the presence of the DBR is enhancing the absorption and collection of photons with energies near the bandgap of GaAs. To further support the qualitative quality of our data, the general shape of the curve was compared to the external quantum efficiency reported by Spire for similar devices. The curves compared very closely in all wavelength regions, indicating that our cells are collecting photons efficiently in all regions of the device.

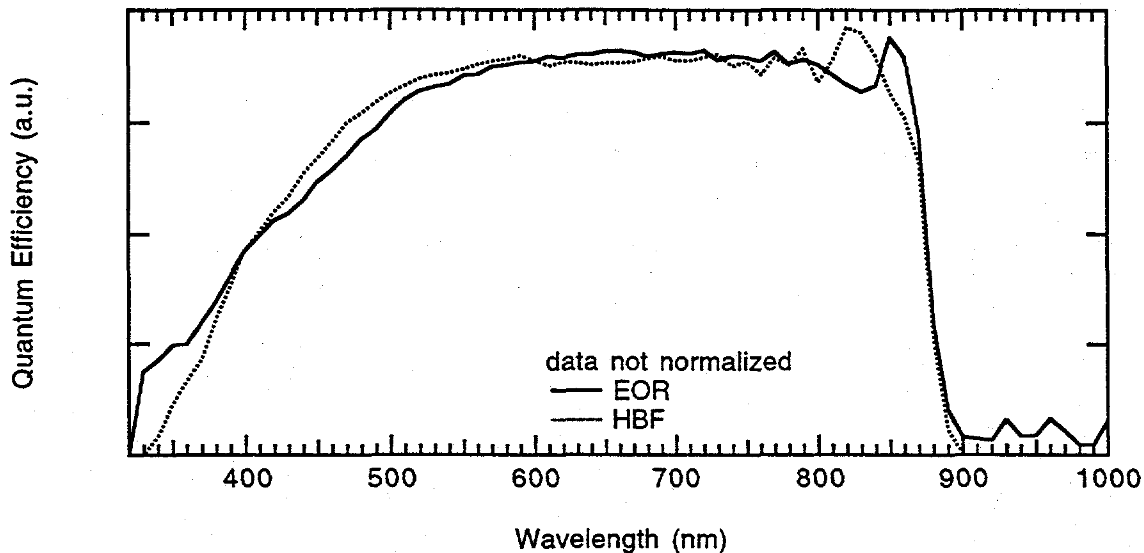

Fig. 40 Quantum efficiencies of representative HBF and EOR cells with normalization

4.0 Summary and Conclusions

This program was designed to test the feasibility of the use of a broad band epitaxial multilayer reflector grown as an integral part of the device structure to reflect the near-band-edge light back through the device for a second absorption pass. The program contained three tasks: 1.) Solar Cell and Reflector Modeling, 2.) Materials Growth and Optimization, and 3.) Solar Cell Fabrication and Characterization. All three tasks were addressed through efforts performed almost exclusively at USC. This was a modification of the original plan. Owing to the withdrawal of Varian from solar cell research, it was necessary to develop all solar cell fabrication and characterization capability at USC from the ground up.

The major accomplishments of this program are:

1) The EOR cell concept was demonstrated and shown to yield solar cells with comparable efficiency for base widths one half the thickness of the standard BSF devices.

2) An in-situ growth rate monitor, laser reflectometry (LR), for the MOCVD growth of complex structures was developed and demonstrated. This monitor was integrated with the reactor control system to allow completely automated growth of GaAs, AlAs, AlGaAs, and complex multilayer structures based upon the input of a structure design and the insitu measurement of GaAs and AlAs growth rates by LR.

3) Low resistance epitaxial Bragg reflectors were fabricated that allow the construction of EOR cells over the entire useful range of AlGaAs compositions.

4) Analysis of the EOR GaAs cell suggests that this design will improve the radiation hardness of space solar cells by a substantial degree, a result that could impact technology choices in space surveillance application area.

There were over 100 epitaxial growth runs performed in support of this work, including 24 samples fabricated into measured solar cell devices. All device results were measured at USC, and they have not spectrally corrected or verified by NREL. We were able to achieve measured efficiencies of 21.5% and 20.0% for HBF and EOR cell designs, respectively, using simulated 1-sun AM1.5G illumination provided by an ELH lamp. Although not as high as the best efficiencies published to date for GaAs heteroface solar cells, these values represent good quality devices. An analysis of the performance parameters leads to the conclusion that our devices are currently limited by high dark currents related to particulate defects and to short circuit currents lower than the best reported values. The fill factors of our cells are excellent, indicating high quality devices with low series resistance. The measured values of V_{OC} are 30-40 mV lower than expected, which we attribute directly to the high saturation current. The values of J_{SC} are also lower than expected, and the ratio of measured to expected values scale with efficiency when compared to the best published devices. Although this suggests the incomplete collection of available photons, there is no evidence to suggest that this occurs in any particular wavelength range or region of our devices. Spectral response measurements show the efficient collection of photons across the full range of wavelengths. The shape of quantum efficiency curves from our devices compare almost identically to the published results for record efficiency cells. The qualitative confirmation of the enhanced collection of near-gap photons was achieved. Unfortunately, data spikes which appear in the band edge region interfere with the quantitative measure of EOR enhancements. There is a possibility that better

performance devices will be represented when our results are confirmed by measurements to be performed at NREL.

We plan to continue our efforts to achieve high efficiency EOR devices. This includes continued efforts in the use of the SimC simulation package to study the behavior of EOR cells with respect to structure, reflector design, and radiation damage. The defects we believe currently limit the performance of our devices are the result of unforeseen hardware failures in our MOCVD reactor which allowed water and oxygen to contaminate the gas handling system. Although the problems have been repaired, the residual effects of contamination have resulted in gradually decreasing but continuing defect generation even during our most recent efforts. Reactor maintenance and modifications designed to remove residual defect generation mechanisms are continuing, and we believe very high efficiency EOR cells will soon result from these efforts.

5.0 Recommendations

The results of this program clearly show that use of a Bragg reflector at the rear of the heteroface cell allows one to decrease the thickness of the base region by a factor of two in a heteroface GaAs solar cell and to maintain high collection efficiency of the cell. The predicted improvements of the cell efficiency over an optimized standard thickness cell are small at 1 sun. It is questionable that the improvements warrant the added complexity of the Bragg reflector for terrestrial GaAs solar cells. However, there is good reason to believe that the EOR cell concept can be used in conjunction with the tandem cell concept to improve the efficiency of these cells. It is often the case that the top, large bandgap cell of the tandem cell is constructed from materials that are less well developed than GaAs and, therefore, exhibit shorter diffusion lengths relative to their absorption lengths than does GaAs. In this case, the ability to use thinner base regions with the same total absorption may allow the cell designer to avoid compromising design tradeoffs that are currently used to optimize tandem cell efficiencies. Our demonstration of low electrical resistance AlAs/AlGaAs Bragg reflectors in this context is an important milestone. It is our strong recommendation that this concept be examined theoretically by NREL or a contractor familiar with materials parameters of AlGaAs or InGaP. The concept of using a rear optical reflector is also useful in other configurations to improve the efficiency of thin film cells.

Perhaps the most important role of the EOR cell may well lie in the improved radiation hardness of GaAs solar cells that is predicted to occur because of the decreased base thickness that is possible with rear optical reflector. The major impact of

this development is on space solar cells where mission life is often controlled by solar cell life. This result has been predicted but as yet untested. It is our hope to be able to test this idea with cells fabricated in this program. It is our strong recommendation that this idea be pursued by an appropriate government agency.

Finally the EOR concept may also be a useful enhancement of the reflection photo cathode designs in that the base thickness again could be reduced by a factor of two perhaps allowing the use of strained layer devices in some applications to increase the wavelength response of the photo cathode.

---

[1] C. Maziar, Masters Thesis, Purdue Univ., 1984
[2] D. E. Aspnes et al, J. Appl. Phys. 60, p. 754 (1986)
[3] Numerical Recipies in C, W. Press, B.P. Flannery, S.A. Teukolsky, W.T. Vetterling, Cambridge Univ. Press, 1988
[4] Berger, Solid State Electronics 15 145 (1972)
[5] T.B. Stellwag et al, Appl. Phys. Lett 56 (17), p. 1658 (1990)
[6] R. Giles, Ph.D. dissertaion, UC Santa Barbara, 1991
[7] M. Tong et al, "A Comparative Study of Wet and Dry Selective Etching Processes for GaAs/AlGaAs/InGaAs Pseudomorphic MODFETs", 1991 Electronic Materials Conference, presentation U6, Boulder, CO
[8] R. Sahara, Ph.D. dissertation, USC, 1991
[9] S.P. Tobin et al, Solar Cells 24 p. 103 (1988)

<table>
<tr><td>Document Control Page</td><td>1. NREL Report No.
NREL/TP-451-5591</td><td>2. NTIS Accession No.
DE93017115</td><td>3. Recipient's Accession No.</td></tr>
<tr><td colspan="3">4. Title and Subtitle
High Efficiency Epitaxial Optical Reflector Solar Cells</td><td>5. Publication Date
August 1993

6.</td></tr>
<tr><td colspan="3">7. Author(s)
P. Daniel Dapkus, Steven G. Hummel</td><td>8. Performing Organization Rept. No.</td></tr>
<tr><td colspan="3">9. Performing Organization Name and Address
University of Southern California
Los Angeles, CA 90089-0483</td><td>10. Project/Task/Work Unit No.
PV321101

11. Contract (C) or Grant (G) No.
(C) XM-0-18110-3
(G)</td></tr>
<tr><td colspan="3">12. Sponsoring Organization Name and Address
National Renewable Energy Laboratory
1617 Cole Blvd.
Golden, CO 80401-3393</td><td>13. Type of Report & Period Covered
Technical Report
1 January 1990 - 31 October 1992

14.</td></tr>
<tr><td colspan="4">15. Supplementary Notes
NREL technical monitor: J. Benner</td></tr>
</table>

16. Abstract (Limit: 200 words)

This report describes work to test the feasibility of a new solar cell concept—the epitaxial optical reflector (EOR) solar cell. This cell concept alters current designs for high efficiency cells by changing the optical absorption efficiency of single cells. The change is introduced by the use an epitaxial multilayer reflector as an integral part of the cell to increase the optical path length of certain wavelengths of light in the cell. These changes are expected to increase the open circuit voltage at which power is extracted from the cell. The program is designed to test the feasibility of the use of a broad band epitaxial multilayer reflector grown as an integral part of the device structure to reflect the near-band-edge light back through the device for a second absorption pass. This second pass allows the design of a solar cell with a thinner base, and the use of the epitaxial reflector as a heterojunction carrier-reflecting barrier at the rear of the device. The thinner cell design and altered carrier profile that results from the light- and carrier-reflecting barrier will decrease the carrier concentration gradient and increase the open circuit voltage. The program is structured to have three tasks: (1) Solar Cell and Reflector Modeling, (2) Materials Growth and Optimization, and (3) Solar Cell Fabrication and Characterization.

17. Document Analysis

a. Descriptors
high efficiency ; epitaxial optical reflector solar cells ; photovoltaics ; solar cells

b. Identifiers/Open-Ended Terms

c. UC Categories
270

<table>
<tr><td>18. Availability Statement
National Technical Information Service
U.S. Department of Commerce
5285 Port Royal Road
Springfield, VA 22161</td><td>19. No. of Pages
51

20. Price
A04</td></tr>
</table>

Form No. 0069E (6-30-87)